VYSOKÉ UČENÍ TECHNICKÉ V BRNĚ
BRNO UNIVERSITY OF TECHNOLOGY

FAKULTA STROJNÍHO INŽENÝRSTVÍ
ÚSTAV MATERIÁLOVÝCH VĚD A INŽENÝRSTVÍ

FACULTY OF MECHANICAL ENGINEERING
INSTITUTE OF MATERIALS SCIENCE AND ENGINEERING

TRANSPARENT POLYCRYSTALLINE CERAMICS AT VISIBLE AND INFRARED WAVELENGTHS
POLYKRYSTALICKÁ KERAMIKA TRANSPARENTNÍ PRO VIDITELNÉ A INFRAČERVENÉ VLNOVÉ DÉLKY

DIPLOMOVÁ PRÁCE
MASTER'S THESIS

AUTOR PRÁCE   Bc. JAN VESELÝ
AUTHOR

VEDOUCÍ PRÁCE   Doc. Ing. MARTIN TRUNEC, Dr.
SUPERVISOR   Dr. YORAM DeHAZAN

BRNO 2010

ABSTRACT

This thesis deals with preparation of transparent ceramic sheets made out of sub-μm alumina powder. Green bodies are prepared by ultraviolet (UV) curing of UV curable resin containing ceramic powder followed by debinding of organic parts at elevated temperature. High relative density of green bodies is essential for reduction of shrinkage during subsequent sintering process. Therefore high solids loading dispersions containing > 57 vol% ceramic particles are used. To reach transparent behaviour, porosity within the sheets must be reduced completely. Therefore hot isostatic pressing (HIP) is used as a final operation. Finally, light transmission and hardness measurements are presented.

Possibilities of making high resolution microstructures using maskless lithography and some suggestions for use of the UV curing technique for production of complex-shaped 3D structures are briefly mentioned.

Keywords: Al_2O_3, UV curing, suspension, dispersion, ceramic sheets

ABSTRAKT

Tato práce se zabývá přípravou průhledných keramických plátů vyrobených ze sub-μm prášku oxidu hlinitého. Zhutnělá keramická tělesa jsou připraveny ultrafialovým (UV) vytvrzováním UV vytvrzovací pryskyřice obsahující keramický prášek s následným vypálením organické složky za zvýšené teploty. Vysoká relativní hustota takto vypálených těles je nezbytná ke snížení smršťování během následujícího slinovacího procesu. Proto jsou použity vysoce plněné disperse obsahující > 57 obj.% keramických částic. K dosažení transparentního chování, porozita uvnitř plátů musí být úplně odstraněna. Proto jako závěrečné operace je použito isostatického stlačování za zvýšené teploty. Nakonec jsou prezentovány měření světelné propustnosti a tvrdosti.

Možnosti výroby mikrostruktur s vysokým rozlišením za použití bezmaskové litografie a návrhy na použití UV vytvrzovací metody pro produkci tvarově náročných 3D struktur jsou krátce zmíněny.

Klíčová slova: Al_2O_3, UV vytvrzování, suspenze, disperse, keramické pláty

This diploma thesis was worked out on the basis of a cooperation between the Institute of Materials Science and Engineering of the Faculty of Mechanical Engineering at Brno University of Technology and High Performance Ceramics Department at EMPA Dübendorf, Switzerland.

Declaration

I declare that this diploma thesis was worked out on my own using mentioned literature and under the supervision of above named supervisors.

In Brno on the 13th of October 2010

……………………………………..

Jan Veselý

Acknowledgements

Table of content

1.   Introduction

There is a rising interest in the world for transparent materials with unique mechanical properties which could be used especially in construction, science, medicine and military sectors. A lot of effort has been already exerted for research on this field. As a result, a number of materials showing transparent behaviour with extraordinary mechanical properties have been developed. Also, many different approaches of processing and shaping of ceramic green bodies have been applied. Among them, ultraviolet (UV) curing technique as one of the wet processing routes represents an approach allowing production of a wide variety of 3D shapes layer by layer, for example by stereolithography. The possibility of curing layer by layer in a very short time makes this method very effective in respect to shaping time, accuracy to shape and finally also cost compared to machining. On the other hand, managing of process chemistry and technology requires optimization of many variables which come out throughout the whole processing and it might be right this reason which hinders a wider use of this technique on the field of ceramics processing. Especially, the large amount of organic binder used here, requires special attention in formulation and debinding procedures. Although, once the complex chemistry is managed, there is a plenty of possibilities opened for its realization.

2. Objectives

This diploma thesis was focused on two objectives. The primary aim was to verify the possibility of making strong and compact alumina windows transparent for visible and infrared spectra of wavelengths. The secondary one, which is unique for this feedstock, was to demonstrate the possibility of making various shapes like extruded thin fibers or high resolution structures using lithography. In both cases UV curing technique was applied.

3.   Theoretical part

At the beginning of this chapter a brief overview of various approaches for production of transparent polycrystalline ceramics made out of several materials is given. Also a principle of preparation of ceramic bodies through UV curing technique is explained. A list of variables is demonstrated. Furthermore, a brief treatise on optics and optical properties of materials with a special insight into alumina are given. Additionally, conditions under which material exhibits transparent behaviour are described. Moreover, grounds for the selection of material are given as well as for the selection of ceramic powder. Two ways of powder stabilization in colloidal systems are shortly presented and colloidal processing of ceramics pointing to our particular processing way is described in details. Finally, sintering and hot isostatic pressing are shortly mentioned.

3.1   Literature overview of transparent ceramics production

In recent years, a number of transparent polycrystalline ceramic materials using different approaches have been developed. Krell et al. report in [1] that transparent spinel (MgO.Al$_2$O$_3$) ceramic was successfully prepared by gel casting and slip casting techniques with consequent hot isostatic pressing (HIP). Thanks to isotropic optical behaviour of spinel ceramic, up to 3 mm thick sheets with a high degree of transparency were prepared. Transparent alumina sheets with thickness of 0.8 mm were also prepared by these techniques. In comparison with optical isotropic spinel, at optical anisotropic alumina the thickness affects transmission of the light significantly. Aluminium oxynitride (AlON) transparent ceramic was made using transient liquid-phase reactive sintering [2] with no final HIP step resulting in almost full transparency at 6 mm thick sheets but grain sizes on the order of 150–200 μm. Also transparent ceramics made out of yttrium oxide (Y$_2$O$_3$) using cold isostatic pressing (CIP) at 200 MPa were produced with an average grain size of less than 1 μm with consequent HIP at 1350°C [3]. Another transparent ceramic prepared out of a mixture of yttrium oxide and aluminium oxide is called yttrium aluminium garnet (YAG) and has been used for lasing systems [4]. Calcined, sintered and HIP-ed YAG ceramics resulted in grain sizes of about 2 μm and a residual porosity lower than 3 ppm. The authors of [5] report a high degree of translucency also at optical anisotropic tetragonal zirconia doped with 3 mol.% of Y$_2$O$_3$ (TZ-3Y) and/or addition of 0.25 wt.% of Al$_2$O$_3$ (TZ-3Y-E) after isostatic pressing and pressureless sintering in air.

As one can see from this short overview, a big number of processing manners can be applied for making transparent polycrystalline ceramics. Not even processing technology but also a possibility of mixing and doping of ceramic powders, which cause structural

modifications, give rise to an immense amount of possibilities how to prepare tailor-made ceramic materials, in this case transparent ceramics.

3.2 Single vs. polycrystalline ceramics

In general, transparent ceramics can be produced as single or poly crystals. Single crystal ceramics can also be made artificially. However, because of its manufacturing demandingness these single crystal ceramics are mostly very expensive which limits their wider utilization. On the contrary, polycrystalline ceramics have, compared to that of single crystals, several advantages. Normally their production costs are not as high as in the case of single crystals and, furthermore, they can be produced by different ways. It means that for different applications can be used different processing approaches. However, for obtaining very fine or high resolution crack-free structures colloidal wet processing is widely investigated.

3.3 General description of ceramics processing using UV curing technique

A colloidal system consists of two separate phases: a dispersed phase and a continuous phase (dispersion medium). In ceramic processing the dispersed phase comprises ceramic nano-scale particles. Such dispersions are then used in sol-gel processes like gel casting. In the gel casting technique the dispersions contain two types of monomers: monofunctional (resulting in linear polymers) and polyfunctional (resulting in cross-linked polymers. When free radical polymerization is initialized, monomers create a polymer network where ceramic particles are trapped. The gelation or polymerization process is initiated by specific initiators sensitive to heat (thermal initiators) or UV (photoinitiators). In our UV curable dispersions, little or no solvent is used. In comparison, the monomers consist only about 15% of the dispersion medium (typically water based) in conventional gel casting. In the case of UV curing, this radical polymerization is initialized after UV light exposure of dispersion with monomers and a photoinitiator. These cured bodies are then submitted to debinding process at which all the organic material in the body is burned out. After debinding, sintering process follows. At this stage ceramic body is densified up to high relative densities. In order to achieve as high level of transparency as possible, residual porosity must be reduced completely. Therefore final HIPing operation is advantageously applied. In the following flow chart (Fig. 3.1), the entire process of making ceramic bodies out of colloidal dispersion using UV curing is depicted.
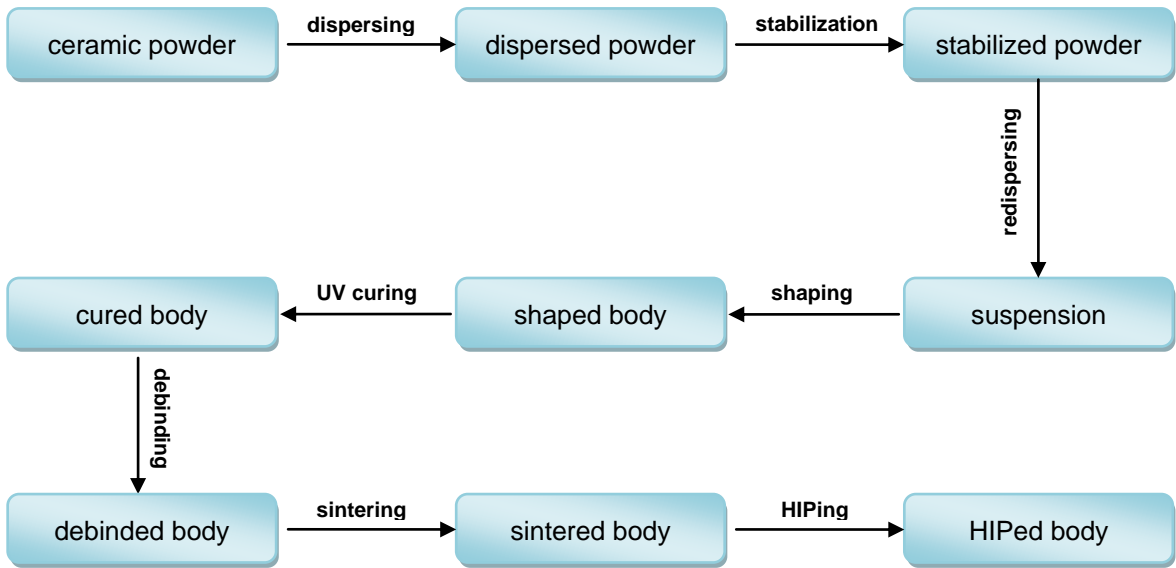
Fig. 3.1   Production process flow chart.

Because of relatively complicated processing, there are many variables which come out throughout the whole process, and which influence more or less the form of final products. For obtaining the best results, in the term of a high level of transparency of final products, these variables must be optimized. It is generally accepted that a very homogeneous and fine microstructure with completely reduced porosity should lead to increased transmittance behaviour of a light beam. A list of variables is demonstrated in the schemes in Fig. 3.2.
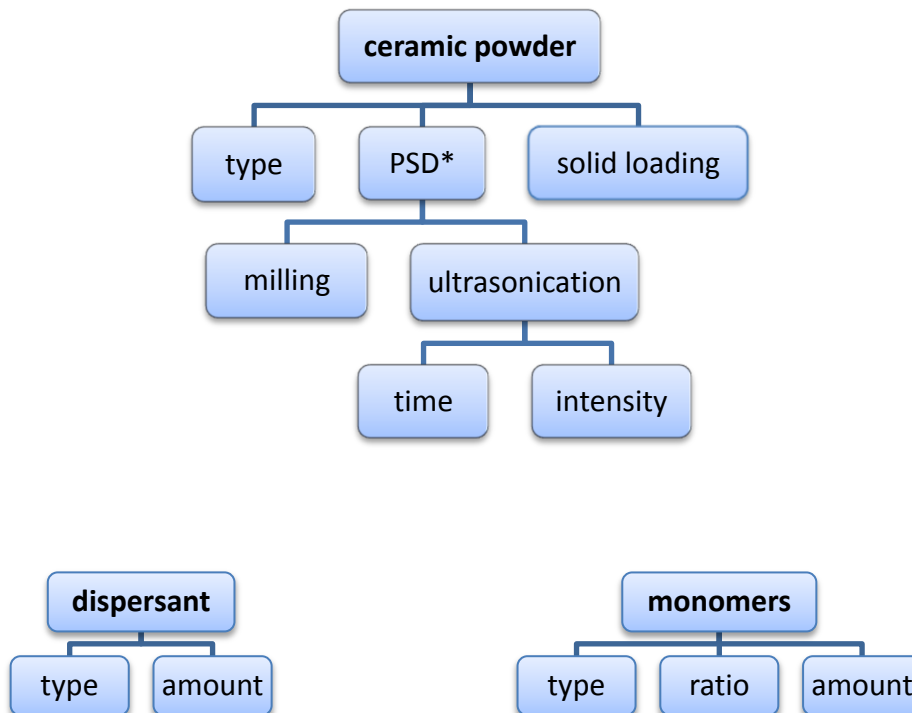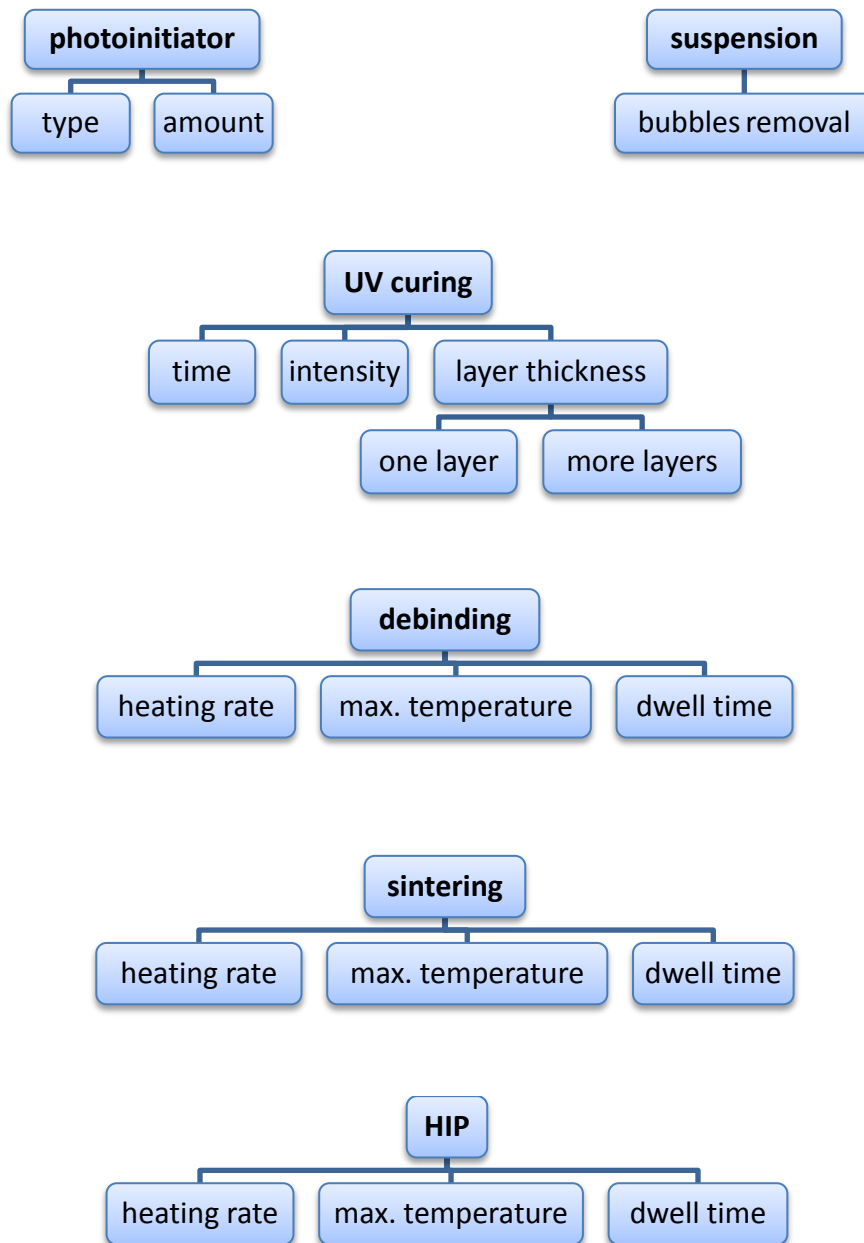
Fig. 3.2   List of materials and process variables.

Taking into account the complicated processing and a number of variables, the initial ceramic material must be chosen wisely and with respect to its theoretical limits. Also the price and availability of ceramic material play an important role. Therefore, in our case, sub-µm alumina powder was chosen as the hardest and strongest material which can be used for transparent compact windows [6]. According to Krell [7], sintered Al_2O_3 exhibits a Vickers macro-hardness HV10 > 20 GPa (at testing load of 10 kgf).

*PSD – Particle Size Distribution

3.4   Determination of concepts from optics

Optics is a part of physics dealing with light. It investigates the essence of light and its interactions with different environments. It is generally known that light represents just a very small part of the spectra of electromagnetic radiation detectable by a human eye. A human eye is capable to detect the wavelengths in the range from 380 to 780 nm. However, wavelengths slightly exceeding, respectively under-riding the visible spectra of wavelengths are also widely used in many applications. These wavelengths are called infrared (IR), resp. ultraviolet (UV). In dependence on transmittance of the light beam through the material, it is necessary to distinguish these three concepts: transparency, translucency and opacity. According to [8], transparent materials are those which are able to provide clear images with a larger distance between the object and the transparent window. While translucent materials are able to provide only a „sharp" image when placed in a very close distance to the object but in a larger distance the image is blurred. Opaque materials do not transmit any light beams.

3.5   Optical properties of materials

Optical behaviour of all materials is, from a physical point of view, a function of optical properties of a material and properties of light. Mutual interactions between light and material can result in various behaviour of a light beam: transmittance, absorption, reflection, fraction and scattering. The vast majority of materials embody a certain combination of some types of behaviour mentioned above. On the basis of this fact, materials can be generally classified as transparent, translucent and opaque. From this point of view, transparency is considered as a material characteristic to transmit light with zero or just a minimal scattering, while translucency is specified as a material characteristic allowing light to pass through partially or diffusely. Opaque materials are those which reflect, scatter and/or absorb light so that no light beam can pass through them. The ability of material to transmit light is strongly dependent on its absorption which is given by chemical composition of the material, and its structure which can contain scattering centres like pores, cracks and grain boundaries. The absorption takes place in absorption centres. These absorption centres are molecular compounds or just atoms able to absorb certain frequencies of light and reflex the others.

3.5.1   Optical properties of alumina

Alumina ceramics exist in a number of different modifications. However, α-alumina is the only stable phase at all temperatures. Its crystal lattice is hexagonal (Fig. 3.3) which

results in anisotropic optical behaviour because of different refractive indexes along *a* and *c* axes. This means that birefringent splitting occurs when the light beam impinges from one crystal to the next [1]. As a consequence of this, the real in-line transmission (RIT) is reduced. According to [9], the RIT is a function of grain size, wavelength and sample thickness and can be theoretically calculated for all birefringent polycrystalline materials. Many authors were trying to improve this RIT by reduction of grain sizes. Hayashi et al. [10] confirmed that the in-line transmission increased significantly at small mean grain sizes (1-2 μm). This corresponds with experimental results of Peelen [11] and Krell [1] who claims that a grain size of 500 nm and extremely dense sintered PCA result in the real in-line transmission of 60% (~70% of theoretical limit) at 1 mm thick sheets measured at a wavelength of λ = 640 nm where maximum transmission is $T_{th} = 100\% - reflection$. He also reports that the thickness, in comparison with isotropic materials, has a significant effect on transmittance at anisotropic materials like α-alumina because of birefringent splitting. In [8], calculations concerning transmittance behaviour of alumina in dependence on the thickness factor were carried out.

Maximal theoretical transmission of alumina can be calculated according to equation (1),

$$T_{th} = (1 - R_t).100\% , \qquad (1)$$

where R_t is a reflection on both surfaces of a window. At normal incidence, the reflection *R* on one surface is governed by the refractive index *n* as

$$R = \left(\frac{n-1}{n+1}\right)^2 , \qquad (2)$$

and the total reflection loss (including multiple reflection) is

$$R_t = \frac{2R}{1+R} . \qquad (3)$$

Thus, the theoretical limit is

$$T_{th} = (1 - R_t).100\% = \frac{2n}{n^2 + 1} \cdot 100\% \text{ [8]}. \qquad (4)$$

In this equation (4), scattering or absorption looses and birefringent splitting is not taken into account so that this equation refers only to alumina single crystal. Also, the reflection on theoretically perfect surfaces is counted here in this equation. As one can see, in these equations (2,4), refractive index *n* of alumina is involved. Refractive index is, in fact, the ration between a speed of light in a vacuum *c* (where it possesses its maximum velocity) and a speed in a given medium *v*, so $n = \frac{c}{v}$. This refractive index is

frequently dependent which means that it will vary in dependence on wavelength used. Usually, the refractive index is measured for a yellow light, where λ = 589.3 nm. According to [12], refractive indexes for α-alumina at this wavelength are n_o = 1.768 and n_e = 1.760, where n_o and n_e are refractive indexes for polarizations perpendicular (ordinary) and parallel (extraordinary). If one of these values is involved in equation (4) the maximal theoretical transmission achieved in a given direction in single crystal alumina will be 85.69 % for n_o = 1.768 and 85.90 for n_e = 1.760 respectively, which corresponds with calculations made in [8].
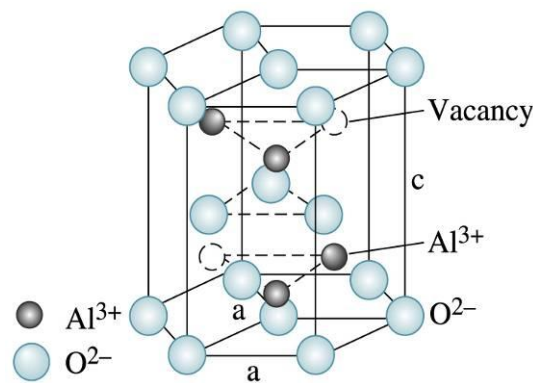
Fig. 3.3   Corundum structure of alpha-alumina (α-AI_2O_3) [13].

3.6   Ceramic powders

Ceramic powders are used in many production processes for making high-performance ceramics. These powders can be characterized by their purity, particle size and chemical heterogeneity. It is generally accepted that these basic powder properties influence significantly further processing and properties of final products. In addition, also packing and distribution of particles control the porosity and microstructure and play a significant role in determining the reliability of final products [14-16]. Therefore it is important to control the packing and particle distribution. For these reasons colloidal processing was developed and successfully applied to a wide range of ceramic systems. In this concept manipulation and controlling of the interparticle forces in powder suspensions are involved [17, 18]. For synthetic powders the ceramic particles usually lie in the submicron range. During processing, these can easily adhere to each other forming secondary clusters which can build up even larger units or agglomerates. These structural heterogeneities can be eliminated if the interparticle forces can be controlled. The chemical nature of the ceramic powder surface is generally of crucial importance in controlling the interparticle forces [19].

3.6.1 Stabilization of ceramic powders

To prevent agglomeration or other structural heterogeneities related to the interparticle forces in colloidal systems, ceramic particles must be stabilized. Attractive interactions responsible for coagulation of the particles are called van der Waals and are electrodynamic in origin as they arise from the interactions between oscilating or rotating dipoles within the interacting media [20]. In order to reduce these attractive forces, the particles must be kept in a certain distance from each other, since these forces get stronger with decreasing interparticle distance. There are several possibilities how to make them stay apart, but only the most universal ones are described here. According to the mechanism used these are called electrostatic stabilization and steric stabilization. Nevertheless, in many cases, stabilization can also be achieved by a combination of both. The stabilization, however, can be carried out only if particles are already well dispersed and ground down in the liquid phase. Therefore, initially, wetting must occur to spread on the powder in the liquid phase. At a later stage secondary clusters and agglomerated particles must be broken down into primary units and finally these primary units or primary particles stay dispersed in the liquid phase [21]. At this stage ceramic particles can be submitted to some type of stabilization.

3.6.1.1   Electrostatic stabilization

The principle of electrostatic stabilization of dispersions consists in creating of a negative charge on the surface of all the particles in the dispersion. This negative charge gives rise to the repulsive forces which subsequently act against attractive interparticle forces when ceramic particles get closer to each other (Fig. 3.4). In dependence on the strength of repulsive and attractive forces, the distance between the particles shifts.
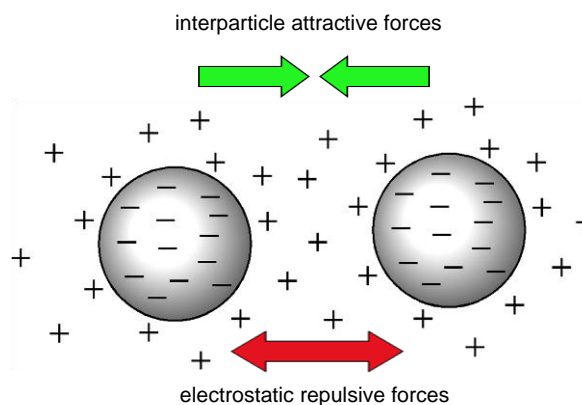
Fig. 3.4   Interparticle action of attractive and repulsive forces in electrostatically stabilized dispersions.

For well dispersed colloidal systems the repulsive forces are such that they keep a certain distance between particles. In the case of strong acting of attractive forces, particles can get so close that they can adhere to each other. Fig. 3.5 illustrates possible particles assembly in dependence on a degree of dispersivity [19].

Dispersed
(non touching network)

Coagulated
(non touching network)

Flocculated
(touching network)
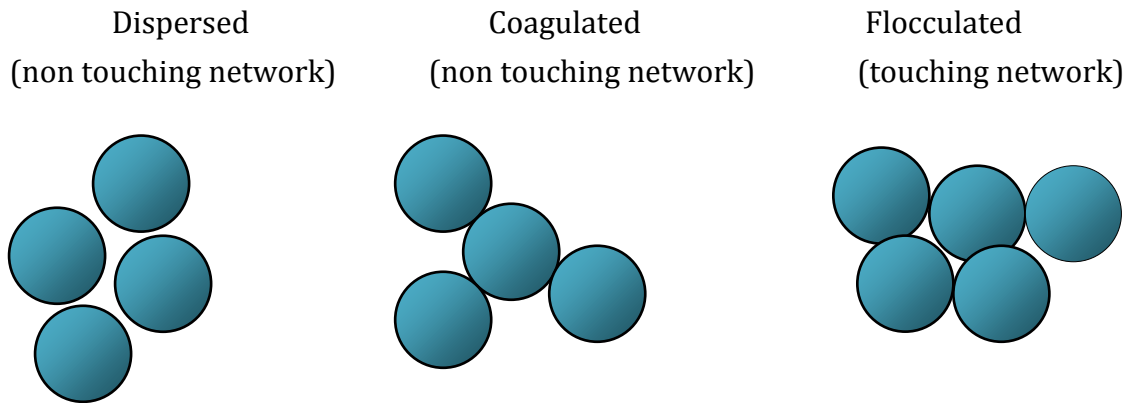
Fig. 3.5   Schematic of the three networks with different degree of dispersivity.

3.6.1.2   Steric stabilization

The principle of steric stabilization lies in adhering of long chain polymers to the surface of ceramic particles (Fig. 3.6). These polymers contain an insoluble functional head group which can be strongly attached to the surface. The tail must have a high affinity for the solvent, so that it can extend then into solution, producing the steric effects required for stabilization. Compared to the electrostatic stabilizing agents, steric stabilizers are less sensitive to ionic strength and are more effective at high solids under extreme flow conditions in both aqueous and non aqueous media [19].
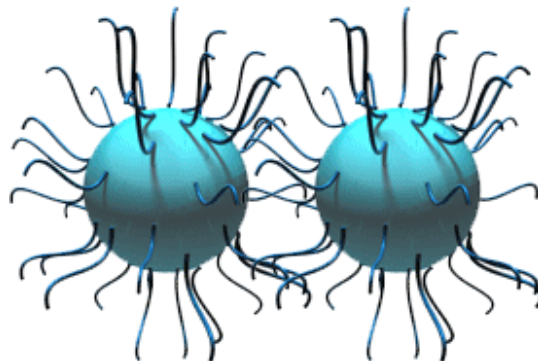
Fig. 3.6   Principle of steric stabilization.

3.7   Colloidal processing of ceramics

Once the ceramic powder has been stabilized it can be used for further processing. In wet colloidal processing, stabilized powder is mixed with organic or anorganic solvents. Incurred suspensions are then shaped and consolidated.

3.7.1   Colloidal processing techniques

Colloidal processing techniques can be divided into two categories: drain casting and direct casting. Drain casting is widely used in the ceramic industry and includes techniques such as slip casting, pressure casting and centrifugal casting. These techniques use a porous mould, which by capillary forces induces a liquid-solid separation to produce a solid green body. This approach, however, has its limitations such as nonuniform densities of the green bodies or restricted possibilities of producing complex-shaped thin-walled components [22]. Therefore, direct casting was developed to overcome the problems of drain casting.

3.7.1.1   Direct casting

The principle of direct casting lies in an in-situ consolidation of the ceramic colloidal suspension in the form without liquid removal. As a result of this a gel-like phase evolves in the form keeping its original shape.

According to the origin of gels, gelation can be classified into two categories: physical gelation and chemical gelation. At physical gelation the network structure is built up from smaller subunits, which are held together by noncovalent bonds – ionic, Van den Waals and hydrogen bonding interactions [23]. At chemical gelation the network structure arises out of developing of pernament covalent bonds between cross-linking and linear monomers [24]. Therefore, chemical gels are generally stronger than physical gels. However, for initiation of the polymerization reaction a suitable initiator must be mixed within the suspension. According to the nature of the initiators, these can be classified to either thermoinitiators or photoinitiators.

3.7.1.1.1   Free radical polymerization

If an adequate type of energy (thermal or light) is brought to the system with initiator, this decomposes to form free radicals. These free radicals start the polymerization of monomers resulting in creation of a polymer network. The description of polymerization reaction is illustrated in Fig. 3.7.

$$I \xrightarrow{\text{energy}} R\bullet \longrightarrow RM\bullet \qquad \text{Initiation}$$

$$RM_i\bullet + M \longrightarrow RM_{i+1}\bullet \qquad \text{Propagation}$$

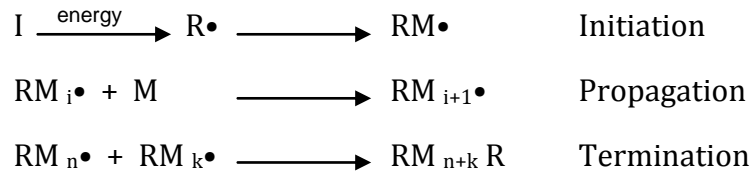$$RM_n\bullet + RM_k\bullet \longrightarrow RM_{n+k}R \qquad \text{Termination}$$

Fig. 3.7   Scheme of free radical polymerization.

Free radical polymerization reaction consists of the three steps: initiation, propagation and termination. At the first step, activation energy is brought to the system and an unstable initiator (I) starts to decompose to form free radicals (R•). Free radicals are molecules with one unpaired electron, therefore they are very reactive. These free radicals serve as active centres from where a polymer chain is generated. Immediately after creating of the first radical, this reacts with an adjacent monomer creating a free radical monomer unit (RM•). At propagation step these incurred units react with other monomers (M) forming a polymer chain. The reaction continues till the two radical monomer units react with each other. At this stage two unpaired electrons from each polymer chain create a bond and the polymerization reaction is terminated.

3.7.1.1.2   Ultraviolet (UV) curable resins

UV curable resins are comprised of a liquid monomer mixture and a photoinitiator. Compared to the gel casting they usually do not contain any aqueous solvent so that UV curable suspension consists only from stabilized ceramic powder, monomers and a photoinitiator. This photoinitiator is sensitive to UV radiation and is able to absorb an UV radiation of a certain range of wavelengths. If the UV curable resin is exposed to UV radiation the photoinitiator starts to decompose forming free radicals which initialize the polymerization. When compared to thermoinitiators, photoinitiators have one drawback if mixed within the colloidal suspensions. While at systems with thermoinitiator bulky components can be cured due to the possibility of homogeneous distribution of heat energy throughout the whole volume, at systems with photoinitiator, its curing ability is closely linked to the light energy coming from the UV light source. This UV radiation is capable to penetrate only to relatively short distances under surface because of energy losses in the material, hence only thin sheets can be fully cured. On the other hand, layer by layer curing is applicable at systems with photoinitiator so that very complicated shapes using rapid prototyping techniques, such as stereolithography, or 3D printing, can be achieved. Fig. 3.8 describes a principle of stereolithography applicable to the UV curable ceramic suspensions.
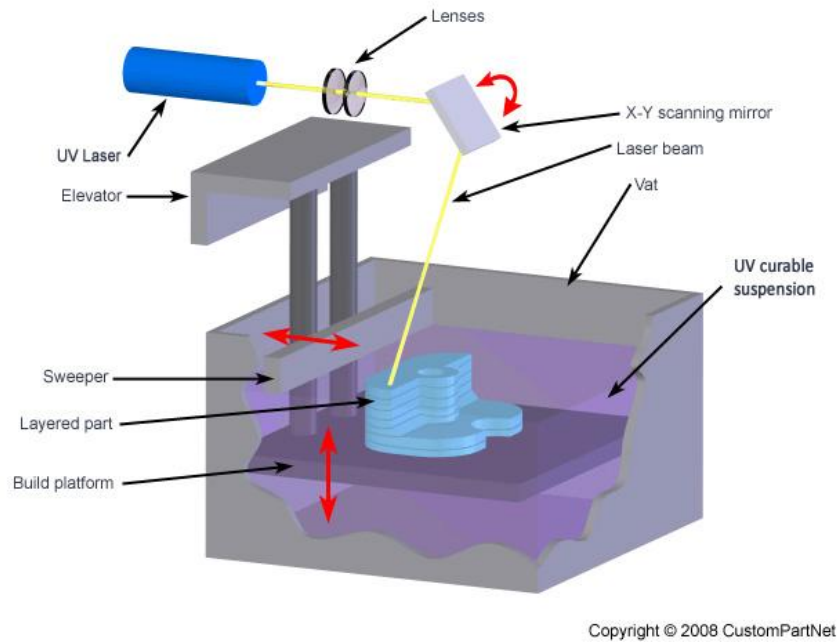
Fig. 3.8 Schematic drawing of stereolithography taken from [25].

3.7.2 Binder burnout – debinding

When the green body has been formed, it has to be dried and all the organic additives must be removed prior to sintering. If some solvent or organic binders remain in the green body at the sintering stage, large volume of gas can be released resulting in cracking or forming bubbles. This processing step is crucial for both, systems with aqueous solvent and systems without it. At systems with aqueous solvent, like gel casting, the drying is the most important step. A big amount of water contained in the green body must be removed which results in a significant shrinkage. As a consequence, cracks can appear. On the other hand, at systems without any aqueous solvent, like UV curable resins, a zero volume of water is replaced by a higher volume of organic part. Therefore debinding step becomes the most important.

Both drying and binder burnout can be controlled by temperature. The heat for evaporation of the solvent and the heat for reaction for binder decomposition control the extent and rate of these processes [20]. The dominating method for removing the organic binders is pyrolysis. It comprises three different mechanisms; thermal degradation, oxidative degradation and evaporation.

3.8 Sintering and HIP

Sintering is a heat treatment of powdered materials which purpose is to densify shaped components up to high relative densities close to the theoretical limit of a given material.

In many cases the densification is accompanied by shrinkage and decrease in component's volume. On the other hand, compact strength increases. Diffusion is the predominant mechanism of mass transfer in the component subjected to sintering. Therefore, with prolonged high-temperature sintering there will be a decrease in the number of pores, the pore shape will become smoother and grain growth can be expected [26].

Hot isostatic pressing is used as a final step in densification process for reducing the residual porosity after sintering. HIP can, however, only be applied when no opened pores are presented within a pre-sintered component since the principle of HIP rests in applying a high pressure of inert gas at high temperature to the surface of pre-sintered component, with the aim of helping the grain growth polarization towards the intergrain regions.

4. Experimental procedure

First chapter of experimental part describes materials used in the process and gives the reasons for their selection. Second chapter gives an overall insight into the processing with detailed procedures, measurements and used instruments.

4.1 Materials

This part is dedicated to all the materials used in the manufacturing process such as powder, dispersing agent, monomers and photoinitiators.

4.1.1 Alumina powder

In order to achieve as much transparency at densified bodies as possible, a suitable alumina powder must be used. Such a powder has to fulfil several requirements. Its purity must be higher than 99.99 % [1]. Its average particle size should be such that would allow the grain size to be lower than 500 nm after densification up to 100 % of relative density. Also, a narrow particle size distribution is desired. According to [1], alumina sub-µm powder with average particle size of 150 nm should be sufficient to this purpose. Therefore, Taimicron TM-DAR sub-µm alumina powder from Taimei Chemicals co., ltd., Japan (TM, α-Al_2O_3, primary particle size ~ 150 nm) was chosen.

4.1.2 Dispersing agent

The election of a suitable dispersant in aqueous or non aqueous media is dependent on solid loading and flow conditions. In aqueous media, in addition, an effectivity of dispersant is strongly influenced by ionic strength [19]. Steric stabilization, in general, offers more effective stabilization at high solids and extreme flow conditions as well as at high ionic strength aqueous solutions. In [27, 28], a successful electrosteric stabilization of alumina powders using comb polyelectrolytes, was achieved in high ionic strength aqueous solutions and UV curable organic monomer mixture. In this work a commercial surface active agent (surfactant) MelPers4343 (MP4343) from BASF, Germany, was used. This syntetic polymer is composed of an anionic low charged density polycarboxylate backbone (sodium salt containing cca 15.5 % of Na) offering electrostatic repulsion and non-charged polyether side grafted chains of 500 g/mol attached to the backbone providing steric stabilization. In order to achieve a good stability of ceramic particles in solvent the backbone part of comb polyelectrolyte must adhere on the surface of the

particles. A schematic of this comb polyelectrolyte is described in Fig. 4.1. The exact system described in [28] is used in this thesis.

grafted chains

backbone
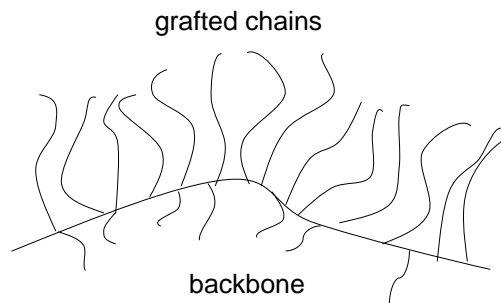
Fig. 4.1   Schematic of comb polyelectrolyte.

4.1.3   Monomers

Two types of monomers must be contained within an UV curable resin to form a polymer network; linear and cross-linking. In [29] several types of monomers were tested as potential UV curable dispersing media for silica nanopowder. Among them, common monomers such as linear monomer butandiol monoacrylate (BDMA) from BASF and cross-linking monomer Poly(ethylene glycol) 200 diacrylate (M282) from Rahn AG were also successfully applied in [28] and were found to be compatible also with sub-µm alumina TM-DAR powder stabilized with comb-polyelectrolytes. Therefore these monomers were also used in our processing. The structure of these monomers is depicted in Fig. 4.2. A mutual ratio between linear BDMA and cross-linking M282 monomers in [29] was 14:1. This ratio was preserved also in this work.

a)   BDMA

b)   M282
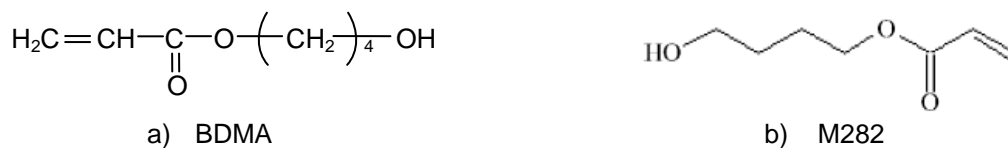
Fig. 4.2   Structure of monomers.

4.1.4   Photoinitiators

Three types of photoinitiators were examined. Two were chosen on the basis of [28, 29]. Solid TPO photoinitiator, with its absorption peak at 380 nm, and liquid LTM photoinitiator containing 25 wt.% of TPO, with its absorption range between 350 and 400 nm.

Later a totally organic photoinitiator MBF, with its absorption range between 250 and 320 nm was tested in this work. All the initiators were received from Rahn, Switzerland. In this thesis, 5 wt.% LTM and MBF and 1 wt.% TPO were used and their influence on density after debinding and sintering was investigated.

4.2 Manufacturing process

In this chapter a manufacturing process with all the measurements is described in details in chronological order. Fig. 4.3 presents a detailed manufacturing process starting with raw ceramic powder and ending with HIPed components.
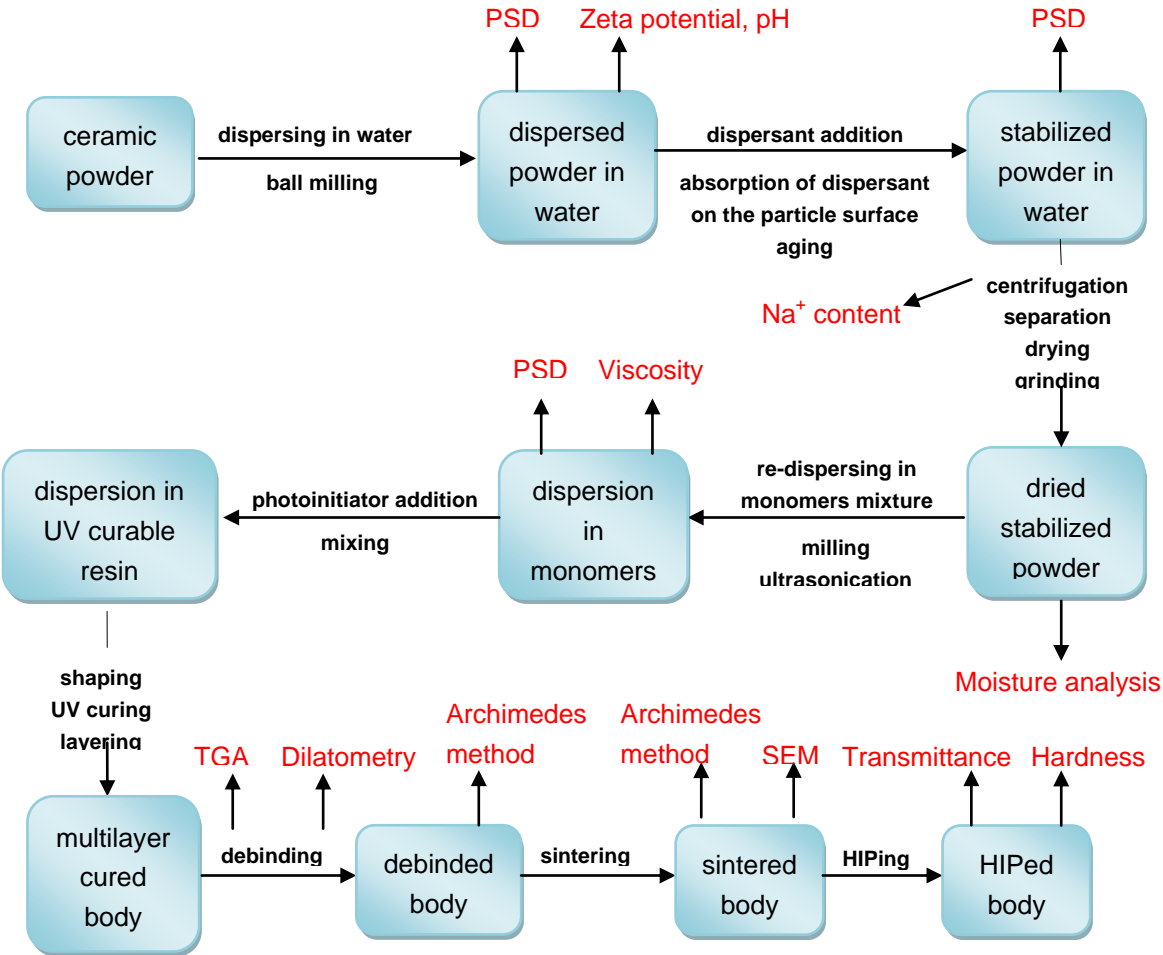
Fig. 4.3   Flow chart of the manufacturing process.

4.2.1   Dispersion in aqueous medium

Stabilization of colloidal ceramic powder can be effectively realized in an aqueous media as was explained in chapter 3.6.1. This, however, requires dispersing of a raw ceramic

powder within an aqueous media beforehand. In aqueous media, agglomerates or even aggregates can be more easily broken down using mechanical forces. Therefore, ball milling or ultrasonication were applied for this purpose. In this work, ball milling of 25 wt.% of alumina powder in deionized water (DIW) was carried out for 24 hours at 60 rpm with Zoz GmbH D 57482 Wenden. Zirconia balls of 0.5 mm in diameter were used as a grinding agent. Particle size distribution (PSD) was checked with Beckman Coulter LS 230 equipped with polarization intensity differential scattering (PISD) curently with milling and when agglomeration was discovered milling continued. When narrow PSD was measured the balls were separated from the dispersion. Once the powder was well dispersed in the water it could be stabilized. However, beforehand, an amount of surfactants on dispersion with 25 wt.% of powder had to be determined. Optimal surfactant concentration was determined prior to this work by zeta potential measurement made during titration of 5 wt.% ceramic dispersion with 7.5 wt.% aqueous surfactant solution by the electroacoustic method (Zetaprobe, Colloidal dynamics, Australia).

4.2.2 Transfer from aqueous to organic medium

Once the powder has been dispersed and crushed down within an aqueous media it can be stabilized. The determined or a bit higher amount of surfactants is added to the dispersion. Residual surfactants which do not stick to the particles can be efficiently centrifuged afterwards. In order to guarantee a good adsorption of surfactants on a surface of the particles the dispersion must be left for 24 hours in this state. After this period, PSD has to be measured to find out if any agglomeration during aging appeared. In case of proven agglomeration, ultrasonication must be used to break down the agglomerates. Once a narrow particle size distribution is achieved the dispersion can be centrifuged (40 min at 10,000 rpm with Centricon H401 - B) to get rid of water and non adsorbed surfactants. Unlike other transform methods (drying), centrifugation is advantageously used for removal of non adsorbed ions such as anionic surfactant's counter ions [28]. These Na^+ ions may act as impurities during sintering. Excess surfactant can negatively influence a re-dispersion in organic media. The Na^+ ions content is measured after centrifugation from a supernatant by flame atomic absorption spectroscopy (F-AAS). Acquired wet stabilized powder is subsequently dried at 60°C for several hours and crushed down in a mortar.

4.2.3 Dispersion in organic medium

Dried stabilized powder is subjected to a moisture analysis with Moisture Analyser HR 83 (Mettler Toledo) and if it is not dried enough the drying is repeated. In other case it is re-dispersed within a monomer mixture and milled in a planetary mill (40 mins at 250 rpm and 15 min at 350 rpm with Retsch PM 400). PSD is measured at this suspension. In case of proven agglomeration, ultrasonication has to be applied and PSD measurement has to be repeated. When narrow particle size distribution is achieved a viscosity of the suspension is measured with a rotational viscosimeter Rheolab MC 120 (Physica Messtechnik GmbH) using cylinder system at shear rates between 10 and 1000 s^{-1} to predict a suitability for shaping process and also a mutual interaction among ceramic powder, surfactants and monomers. Measurements which were repeated three times consisted of 20 measurement points across the mentioned range of shear rates with logarithmic progression. Further, a photoinitiator is added to the suspension and mixed. At this point it is important to wrap a vessel in an aluminium foil so that no light could penetrate into the vessel and initiate a decomposition of the photoinitiator. Incurred dispersion in UV curable resin is further shaped.

4.2.4 Shaping

Prepared UV curable suspension contains entrapped air bubbles arose from mixing. These bubbles must be removed before shaping. Therefore two approaches of bubbles removal were used – vacuum degassing and screening through a 180 μm sieve. Bubbles-free suspension was then used for shaping process.

Primary aim of this thesis was the preparation of transparent PCA ceramic sheets. These sheets were prepared by casting and planarization by rolling between two plastic foils. Plastic foils can influence a surface quality of cast sheets. Furthermore, entrapment of bubbles may occur at this stage. Therefore two types of plastic foils were used and their influence on surface quality was examined; a 125 μm thick polypropylene foil and a foil for printing from 3M™. The structure of the foils was examined with Light Microscope Leica DM2500 M. Monolayer and multilayer casting were performed and their influence on relative density of debinded and sintered bodies was investigated. The thickness of the sheets was in both cases 1 mm.

To demonstrate the possibilities and advantages of UV curing also other shapes such as fibers and high resolution microstructures were prepared. Fibers with thickness of 300 μm were extruded manually using extrusion syringe and UV cured in water. High resolution microstructures were shaped with lithograph SF-100, Intelligent micro pat-terning, LLC.

4.2.5 UV curing

Cast sheets were put into a curing chamber UV cube 100 equipped with a 100W Fe lamp (Dr. Hönle UV Technology, Germany) providing 120mW/cm^2 (significantly broadband) radiation spectrum in the UV area, with its main peak at 360 nm and exposed to UV radiation for 2 minutes. In case of multilayer structures this process was repeated for each layer separately.

4.2.6 Debinding

At debinding step, the organic material in the cured green body is burnt out. Due to a relatively high concentration of organics in UV cured green bodies, this is a critical step in the term of a possible damage of debinding component. Therefore the heating rate and maximal temperature must be chosen wisely. Therefore several debinding regimes were applied to optimize this critical step. Debinding process was realized in PYROTEC Brennofenbau Osnabrück (model PY 12 H 1300°C) furnace which allows very slow heating rates. In order to get information about burning process, thermogravimetric analysis (TGA) and differential thermal analysis (DTA) measurements were performed with TGA/DTA 851, Mettler Toledo. Dilatometry measurements were done to investigate the influence of heating rate on shrinking during debinding using BÄHR Thermoanalyse GmbH (model Dil802S1). Relative density was measured at debinded samples using Archimedes method with AG204 DeltaRange, Mettler Toledo. As a theoretical density of alumina was used ρ_{th} = 3.987 g.cm^{-3}.

4.2.7 Sintering

Sintering of debinded components was performed in Carbolite HTF 1700 furnace. Different sintering regimes were applied with the aim of reaching closed porosity and as small grain sizes as possible. Both one step and two step sintering were used for densification process and their effect on final microstructure was investigated. Besides, also pre-coarsening heat treatment was studied and its influence on density and grain size was examined. Relative density was measured at sintered components with Archimedes method. Microstructure of sintered components was observed with scanning electron microscope (SEM) Tescan VEGA Plus 5136 MM. Average grain sizes were estimated from SEM pictures by intersectional method. The number of grains was counted along 6 line segments of known distance and an average value was calculated.

4.2.8 HIP and final measurements

HIP was carried out to reduce residual porosity within the sintered components. Two HIP regimes were used. Firstly at 1400 ℃ for 4 hours at 200 MPa and secondly at 1200 ℃ for 2 hours at 198 MPa. It is important to note that the HIP runs were intended for materials from other projects. The HIP conditions used were therefore not at all optimal for the aluminas produced in this thesis. Final density was measured with Archimedes method. Also transmittance of light in visible and IR spectra was measured at 1 mm thick sheets with Varian Cary 50 UV-Vis Spectrophotometer. Vickers microhardness measurement was performed with Ernst Leitz GmbH D-6330 Wetzlar, with 1 and 2 kg loading.

5.   Results and discussion

This chapter summarises the results of all the measurements and gives explanations or comparisons in a form of discussion. A big attention is paid especially to the preparation of dispersions and description of achieved microstructures.

In chapter 3.3 a list of variables is demonstrated. Here, studied variables are presented. These variables can be divided into process and quality variables. A list of studied variables with their baselines in our processing is presented in Table 1a, 1b.

Table 1
A list of studied

a)   process variables

Process variables	baseline
Solid loading (nominal)	42 vol%
Photoinitiator	LTM
Layer thickness	1x1000 μm
Debinding rate	0.9 °C/min
Max. debinding temperature	650 °C
Sintering temperature	1500 °C
Sintering dwell time	2 h
HIP temperature	-
HIP dwell time	-
Washing prior to sintering	-
Washed and re-centrifuged powder	-
Solvent addition	-

b)   quality variables

Quality variables	baseline
Vacuum degassing	-
Sieving	-
Substrate foil	polypropylene

Optimization of variables listed in Table 1a, 1b was performed. Achieved results are presented by topics/variables but not in chronological order. A comparison between baselines and achieved results is made at the end of chapter 5.

5.1 Preparation of high loaded dispersions

The concepts and optimization of the alumina powder dispersion in water and curable monomer were developed in previous works [28,30]. The development continued in this thesis to prepare high-loaded dispersions (57 vol%), solvent containing dispersions and improved re-dispersion after washing of centrifuged powders. Ceramic powder was at first dispersed and then stabilized in DIW. Thanks to a good solubility of used surfactants in both water and monomer mixture, a transfer from the aqueous medium into the organic one could be advantageously applied in terms of washing (or centrifuging) out the impurities or residual non adsorbed surfactants. Finally this re-dispersion (in organic medium) was mixed with photoinitiators creating an UV curable suspension.

5.1.1 Stabilization of ceramic powder in water

Particle size distribution was measured at 25 wt% TM-DAR powder dispersion in deionized water after ball milling with zirconia balls. Fig. 5.1a describes measured PSD of dispersed powder in DIW.
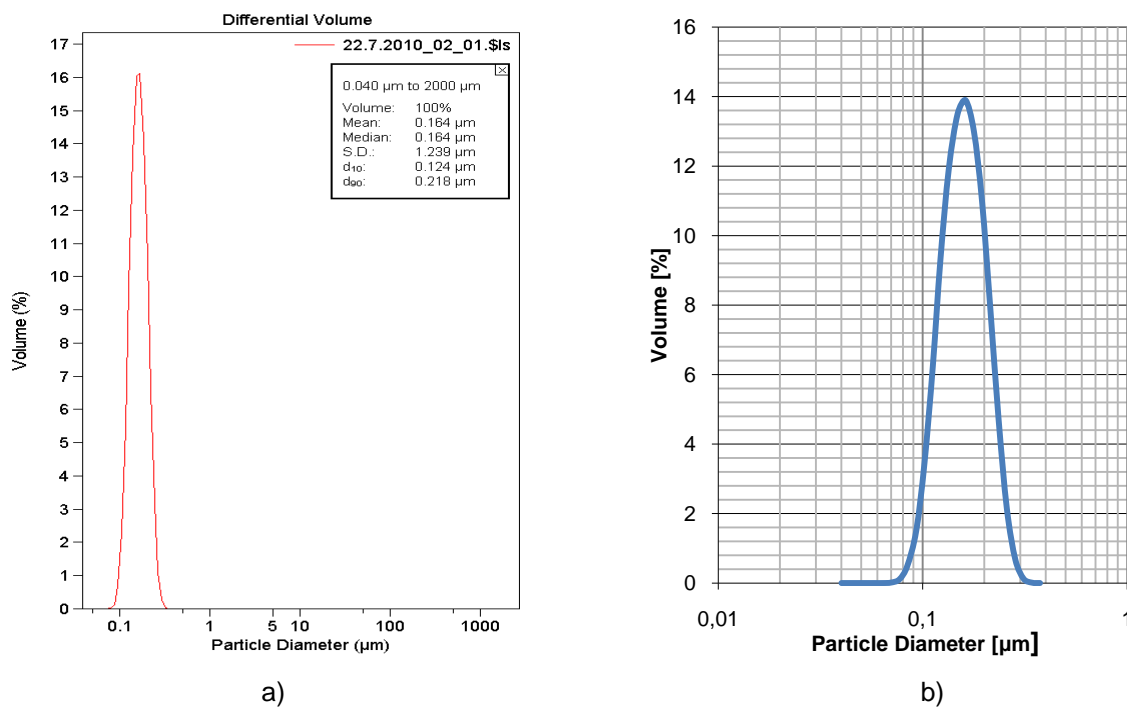
Fig. 5.1 PSD of a) dispersed powder in DIW and b) dispersed powder in DIW with 4.5 wt% Melpers.

Dispersed powder in DIW could be further subjected to steric stabilization. Fig. 5.1b describes PSD of dispersed powder in DIW with 4.5 wt% Melpers surfactants. The de-

crease in volume at the peak of PSD in Fig. 5.1b compared to the PSD in Fig. 5.1a can be caused by the presence of surfactants which are stuck to the particles.

For a good adsorption of surfactants on the surface of particles it is important to know how the pH of dispersing medium influences a charge on the particles, in other words, how the pH influences zeta potential of the dispersion. Therefore zeta potential measurement of dispersed powder in DIW was performed. Zeta potential was measured in a pH range from 3 to 11. At first the dispersion was titrated from its natural pH in DIW (pH of 5) to a pH of 11 (called "first leg") sodium hydroxide and then down to a pH of 3 (called "second leg") with hydrochloric acid. Fig. 5.2 depicts a dependence of zeta potential on pH.
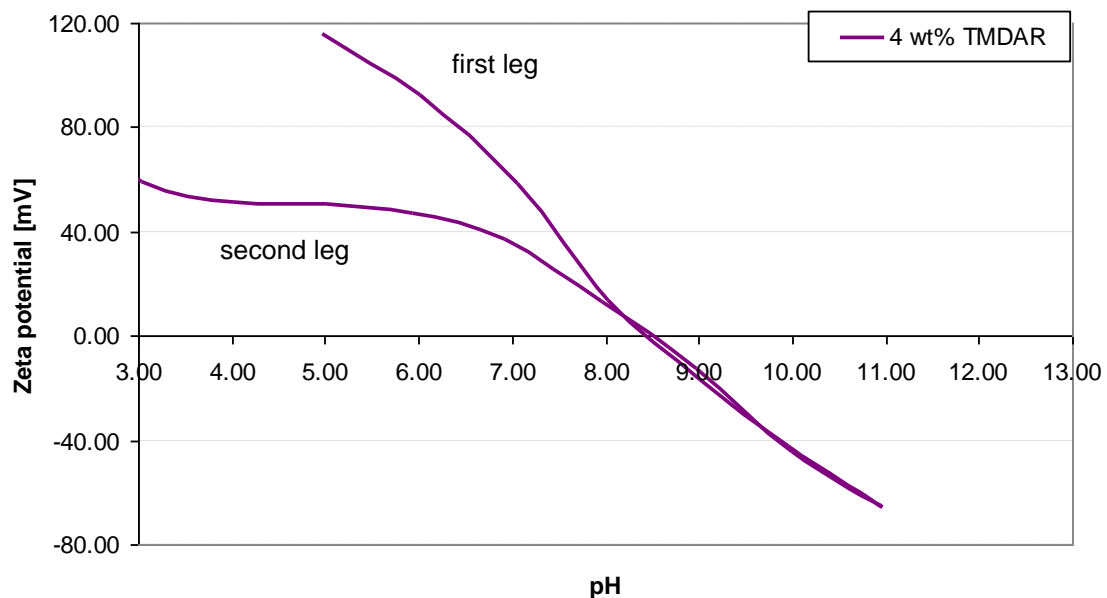
Fig. 5.2   Zeta potential of TM-DAR powder dispersed in DIW.

The value of isoelectric point (IEP) for TM-DAR powder in DIW was at pH of 8.4. At natural pH in DIW the zeta potential was positive which means that the surface of particles was positively charged. Positive charge on the particles allows adsorption of small anionic surfactants such as carboxylic acids [31] and comb-polyelectrolytes [27] due to electrostatic attraction. The amount of surfactants has to be determined. Therefore zeta potential measurement made during titration of 5 wt% powder dispersion with 7.5 wt% aqueous surfactant solution was performed. Fig. 5.3 describes a dependence of zeta potential and pH on the amount of surfactants.
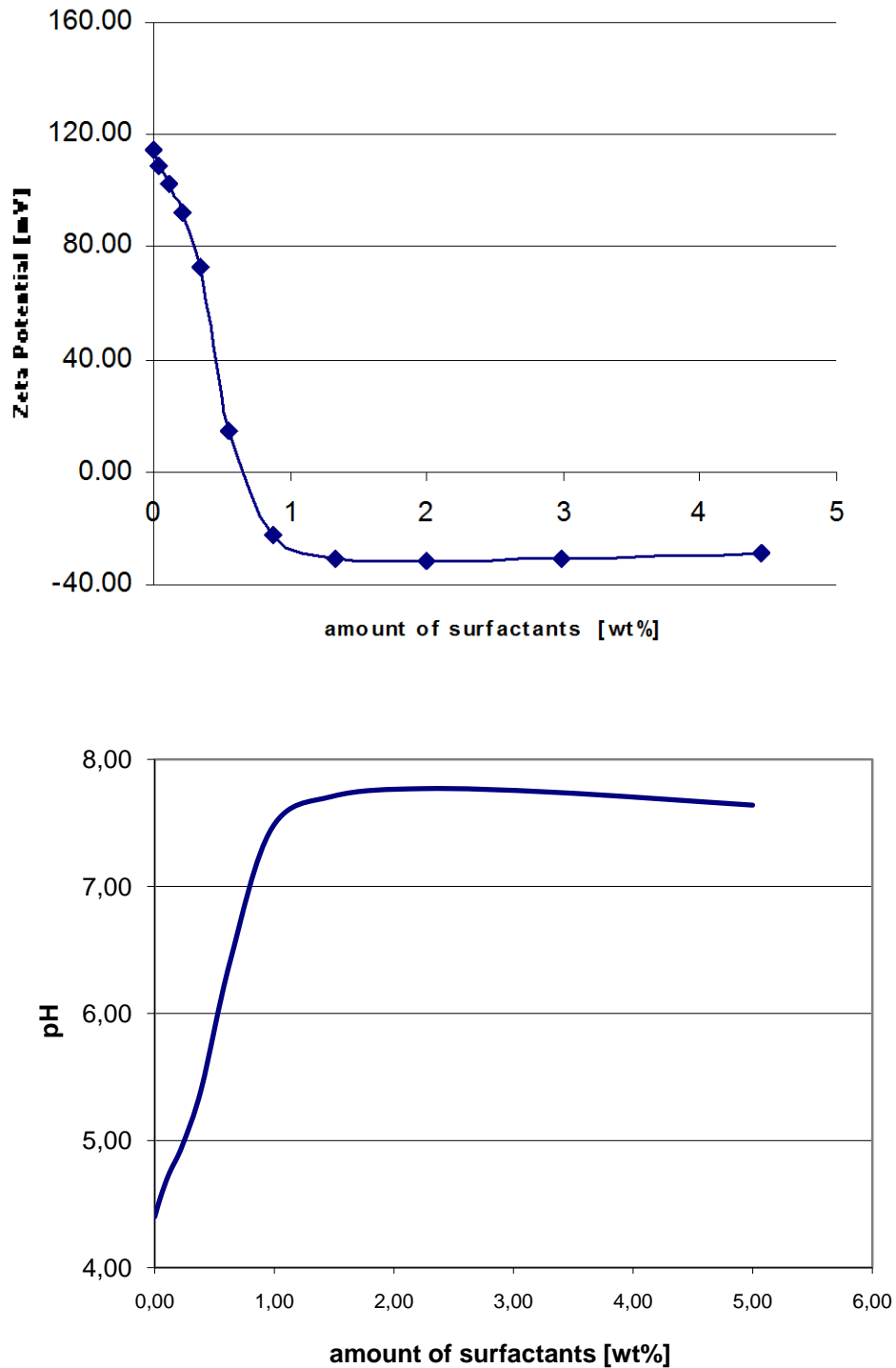
Fig. 5.3 Plots of zeta potential and pH dependence on the amount of added surfactants.

The amount of added surfactants is related to the amount of powder in 5 wt% dispersion. From graphs in Fig. 5.3 implies that a significant decrease of zeta potential followed by depolarization of the charge on the surfaces of particles and subsequent growth of negative charge, and at the same time increase in pH, took place during addition of only 1 wt% of surfactants. One can also see from these graphs that after cca 2 wt% surfac-

tants addition, zeta potential is not being changed or it is being changed only very slowly in the direction of zeta potential detraction. This might indicate that powder is already stabilized after addition of 2 wt% of surfactants and the rest of surfactants are not adsorbed on the particles. However, all the particles do not have to be stabilized in such a short time in which this measurement was performed (15 min). Therefore, to be sure that all the particles can be covered with adsorbed surfactants and in discussion with [27, 30], 4.5 wt% of surfactants was finally added into the dispersion. Non adsorbed surfactants are expected to be centrifuged out along with water and impurities in further processing.

In order to acquire information about a real amount of adsorbed surfactants on the particles, TGA of centrifuged and dried powder with adsorbed surfactants was carried out and compared to TGA of pure powder (with no surfactants). This graph is shown in Fig. 5.4.
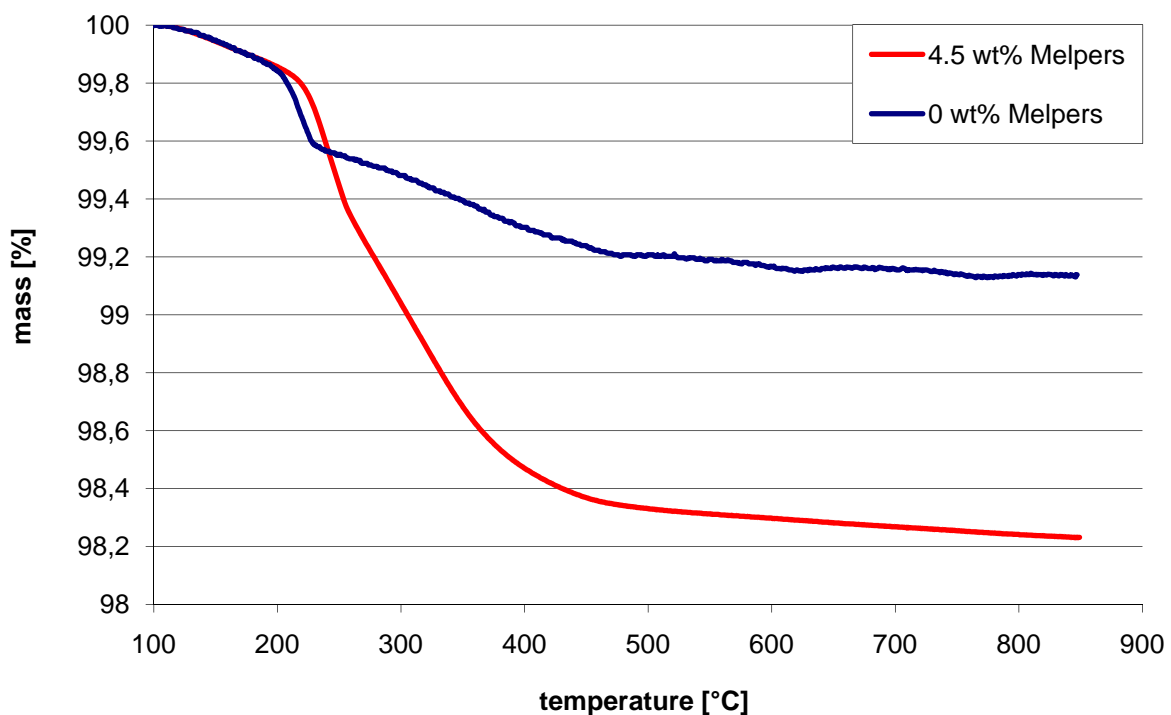
Fig. 5.4   TGA of powder with and without adsorbed surfactants.

As one can see from Fig. 5.4 a decrease in mass of cca 0.85 wt% at 800 °C was also recorded for pure powder with no surfactants (blue line). It is assumed that some residual moisture could be evaporated at lower temperatures (100 – 200°C), however, next mass loss remains a question. A maximum mass loss of powder with 4.5 wt% of surfactants at 800 °C was 1.75 wt%. However, if the mass loss achieved for pure powder at 800 °C is subtracted from the maximal mass loss of powder with surfactants, a minimum mass

loss can be calculated. Therefore a minimal mass loss for powder with 4.5 wt% of surfactants was 0.9 wt%. However, it has to be mentioned here that because of anorganic content in Melpers (Na salt), both values have to be corrected. Then the minimal and maximal values would be 1.1 wt% and 2.1 wt% respectively. This range corresponds to the assumption made on the basis of zeta potential measurement during surfactants titration. This TGA measurement also proved that non adsorbed surfactants were successfully centrifuged. On the basis of [28], where the measurement of undesirable surfactant counter ions (Na^+) content in supernatant after centrifugation was carried out, it was found that the Na^+ content can be effectively centrifuged. Fig. 5.5 illustrates the influence of centrifugation on decrease of Na^+ content.
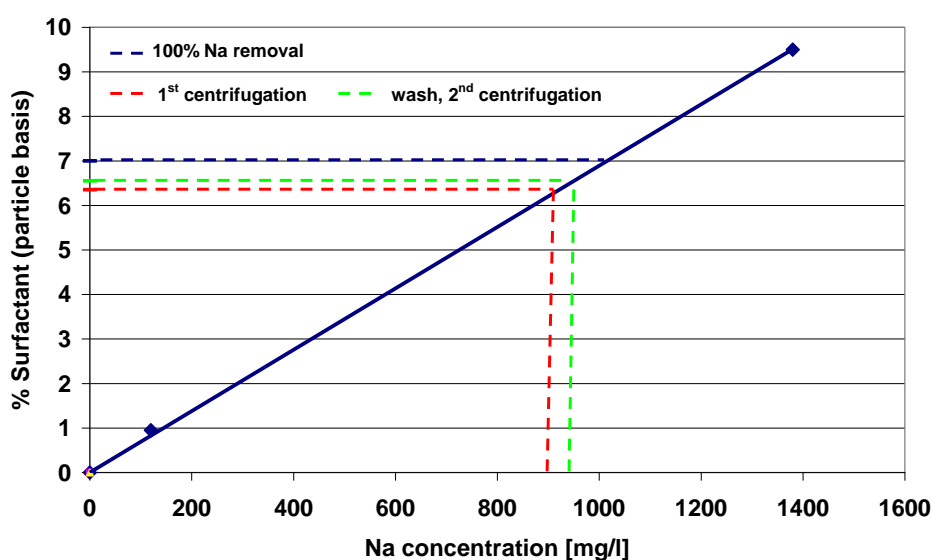
Fig. 5.5   The separation of Na^+ ions during centrifugation. Taken from [28].

The blue line in the graph in Fig. 5.5 represents a calibration curve obtained by measuring the Na^+ content at solutions with known surfactant concentration. The Na^+ content of a supernatant obtained after centrifugation of the dispersion with 7 wt% of surfactants is represented by dashed red and green lines. After first centrifugation the content of Na ions in supernatant corresponds to 6.4 wt% surfactant and therefore > 90 wt% Na removal by centrifugation. Second centrifugation even improved the content of centrifuged Na ions to 94 wt%.

5.1.2   Stabilization in the monomer mixture

After centrifugation the deposit is dried and crushed down with a pestle and mortar. The moisture content is checked after drying and typically lower than 0.5 %. The dried pow-

der with adsorbed surfactants can then be dispersed in mildly polar organic media, such as the UV curable 14:1 BDMA/M282 monomer mixture [28, 29].

5.1.2.1 Nominal and real solids loading

Stabilized powder was mixed with monomers in three different ratios which are presented here in nominal solids loading as 42, 50 and 57 vol%. These ratios are, so called, nominal because they represent only an initial ratio between the stabilized powder and monomers. These ratios do not take into account a volume of adsorbed surfactants on the particles surfaces and also do not include later photoinitiator addition. The real solid loading (containing surfactants and photoinitiators) can be precisely determined after TGA measurement at which the organic part contained in the cured body is completely burnt out. TGA measurement for this purpose was carried out for cured bodies with 57 vol% solid loading resulting in cca 19 wt% loss which, after calculations, corresponds to cca 4 vol% loss in respect to initial solid loading so that the real solid loading was cca 53 vol%. Fig. 5.6 shows the TGA of the 57 vol% dispersion.
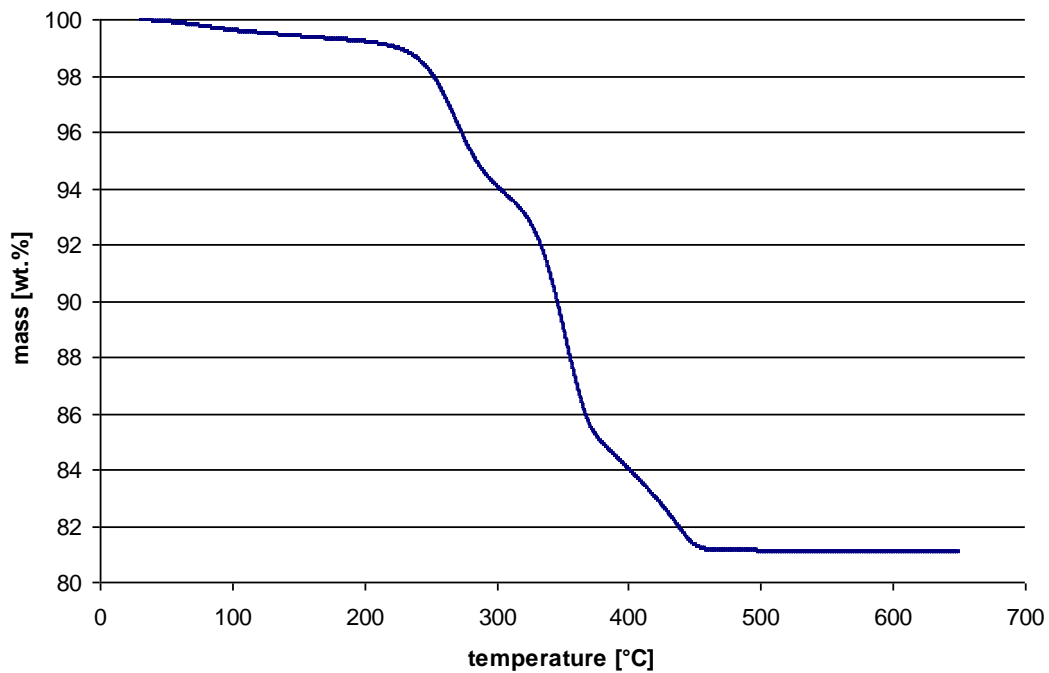
Fig. 5.6   TGA of the 57 vol% dispersion.

5.1.2.2 Particle size distribution of re-dispersed powder

Particle size distribution was checked after re-dispersion of stabilized powder in the monomer mixture. Fig. 5.10 shows a) badly and b) well re-dispersed powder in monomers.

a)   relatively bad re-dispersion   b)   good re-dispersion
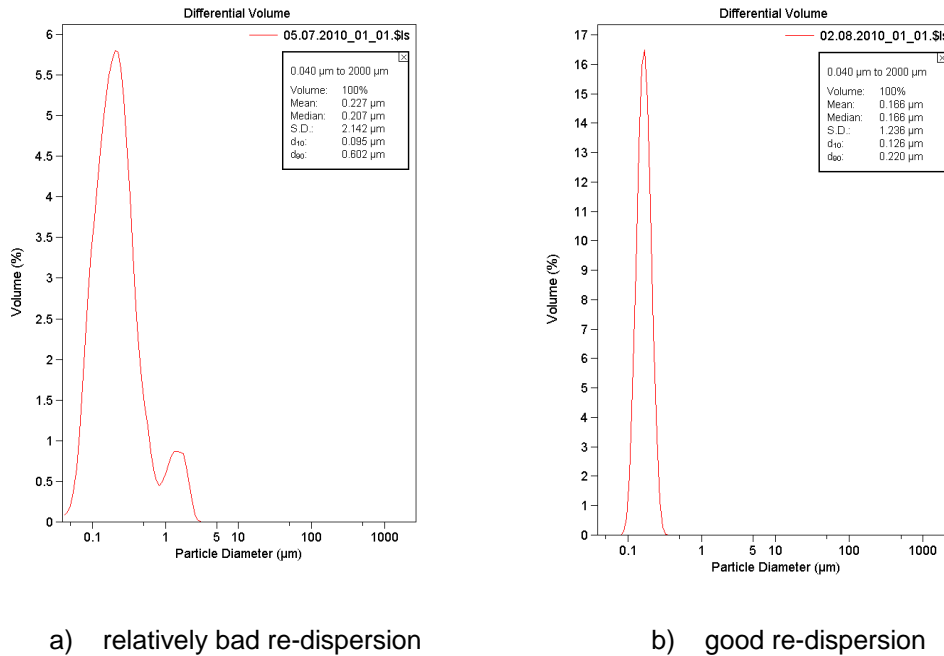
Fig. 5.10   PSD of re-dispersed powder in the monomer mixture.

PSD of re-dispersed powder was mostly unsatisfactory after planetary milling, therefore ultrasonication had to be applied to break down the agglomerates. Only after washing of the stabilized powder, the PSD was always good so that ultrasonication did not have to be applied. The effect of washing is discussed in chapter 5.2.

5.1.2.3 Rheological measurements

To determine a suitability of suspensions with different solids loading for further shaping process and also a mutual interaction among monomers, powder and surfactants, viscosity measurements of 50 and 57 vol% solids loading were made.

It has to be noted here that these viscosity measurements were performed for dispersions before addition of liquid photoinitiators which dilute the dispersions so that a real viscosity (with photoinitiators) should be even lower than is presented here in Fig. 5.7. It has to be also mentioned that in case of 57 vol% solid loading dispersion, the stabilized powder was washed once more after centrifugation and then centrifuged one more

time. The effect of powder washing and re-centrifuging on further processing is discussed in chapter 5.2.
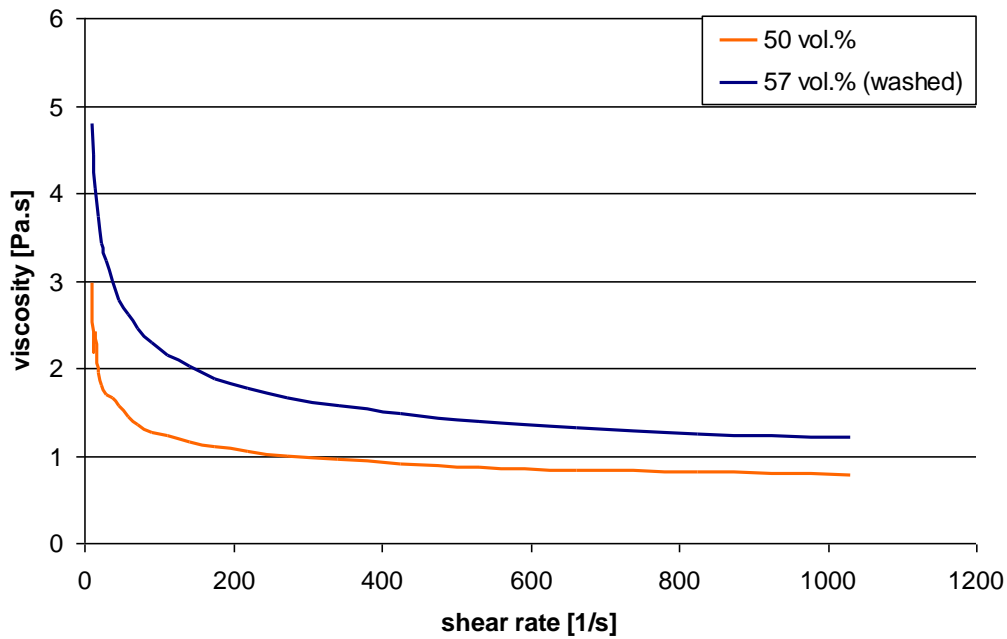
Fig. 5.7   Viscosity measurements of 50 and 57 vol% solids loading.

As one can see from this graph, the viscosities rise very slowly from a shear rate of 1000 s^{-1} up to a shear rate of 200 s^{-1} and a shear thinning behaviour can be observed in this range. Shear thinning exponents which indicate a type of dispersion behaviour were calculated from equation (5)

$$\tau = K.\dot{\gamma}^{n}.$$ (5)

, where τ is a shear stress, K is a specific pre-exponential factor, γ is a shear rate and n is a shear thinning exponent. If $n < 1$, dispersions embody a shear thinning behaviour while if $n > 1$, dispersions embody a shear thickening behaviour. A shear thinning exponent of 1 indicates Newtonian behaviour. In mentioned range average shear thinning exponents were calculated for both 50 and 57 vol% dispersions resulting in n = 0.81 and n = 0.75 respectively. Shear thinning behaviour is favourable for casting the layers (e.g. tape casting) [32]. The relatively weak shear thining behaviour seen here testifies to the well dispersed nature of the dispersions. At a shear rate of 100 s^{-1}, the viscosity of 57 vol% solid loading is almost twice as high as in case of 50 vol% solid loading. At shear rates lower than 100 s^{-1}, both viscosities rise rapidly and shear thinning exponent decreases. Between shear rates of 10 and 100 s^{-1}, average shear thinning exponents for 50 and 57 vol% dispersions were n = 0.63 and n = 0.67 respectively.

As expected, viscosities increased with increasing solid loading reaching 3.23 Pa.s at 57 vol% dispersion and 1.7 Pa.s at 50 vol% dispersion at a shear rate of 30 s^{-1}. These values are still below a maximum recommended limit for stereolithography applications (< 5 Pa.s at 30 s^{-1} [33]). On the basis of these measurements, finally 57 vol% solid loading dispersion was chosen for further processing.

The influence of temperature on the viscosity of the 57 vol% (53 vol% respectively) solid loading dispersion was studied. The influence of three different temperatures (10, 23 and 40 °C) was examined and showed in Fig. 5.8.
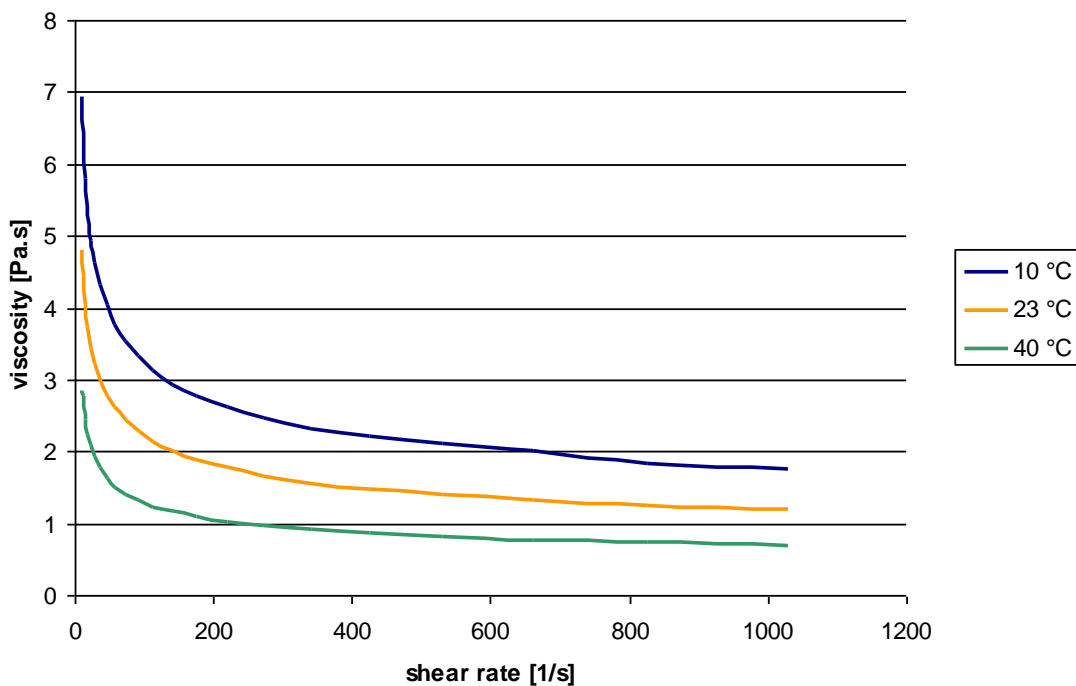
Fig. 5.8   Influence of the temperature on viscosity of 57 vol% solid loading dispersion.

Increasing temperature influences a viscose behaviour of the dispersion. It was found that viscosities decrease with increasing temperature. Therefore, it can be expected that the monomer mixture viscosity decreases with increasing temperature. In order to explore the nature of the viscosity reduction with increasing temperature, viscosities of the 57 vol% dispersion measured at different temperatures (10, 23, 40°C) were compared to the viscosities of pure monomer mixture measured at the same temperatures. The ratio between dispersion viscosity and monomer mixture viscosity is called reduced (relative) viscosity as presented for example in references [34, 35, 36]. The reduced viscosity with increasing temperature directly shows a trend in viscosity shift between monomers and particles. The dependence of reduced viscosity on temperature at a shear rate of 531 s^{-1} is shown in Fig. 5.9. It has to be mentioned here that a value of re-

duced viscosity is dependent on a shear rate (since the monomer shows Newtonian behaviour), therefore for a description of overall behaviour of a dispersion viscosity, however, the dependence of reduced viscosity on temperature is the focus here. In this work a shear rate of 531 s^{-1} was chosen as a comparative value for all the measurements.
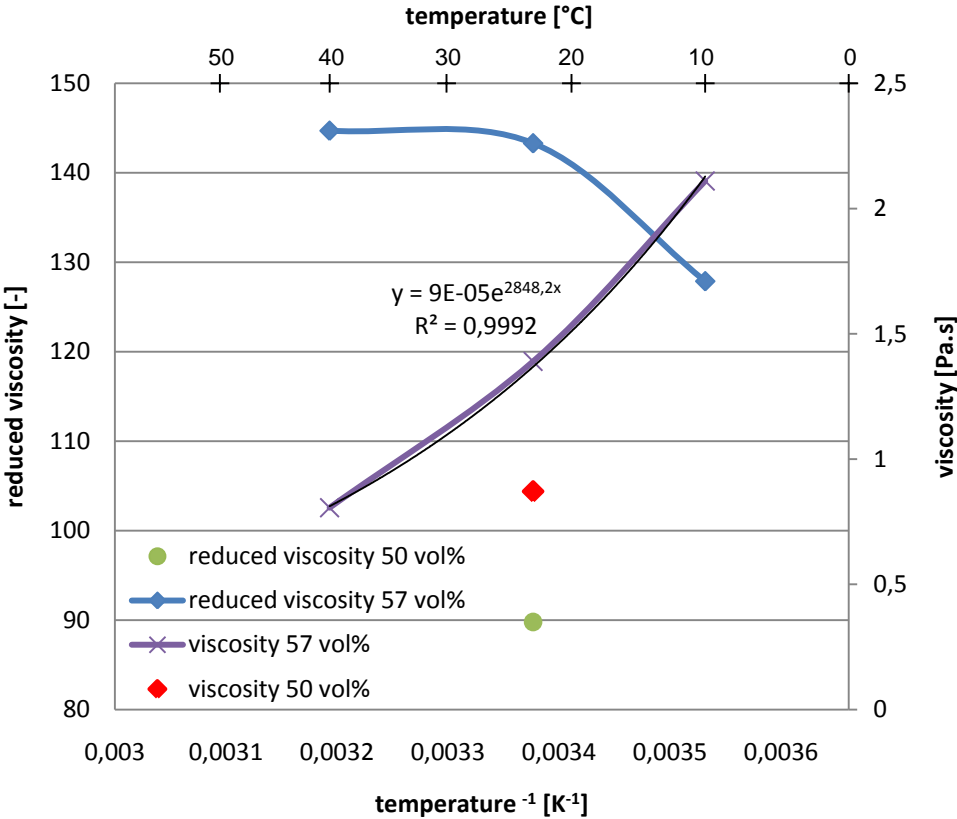
Fig. 5.9   Viscosity and reduced viscosity of the 57 vol% and 50 vol% dispersions as a function of temperature at a shear rate of 531 s^{-1}.

As one can see from the picture (Fig. 5.9), the reduced viscosity did not change a lot within the mentioned temperature range. It was reduced by only a factor of 1.13 at a shear rate of 531 s^{-1} by heating from 10 to 40 °C. This means that the change of dispersion viscosity is almost entirely a function of the change of monomer mixture viscosity in dependence on the temperature change. This means that the dispersion viscosity decreases with rising temperature proportionally to the viscosity of the monomers mixture which confirms our expectations. In other words, even at 57 vol%, no significant particle-particle interactions take place.

In Fig. 5.9 also can be seen a rate of the viscosity increase for 57 vol% dispersion. The reduction of viscosity by a factor of 2.6 was observed by heating from 10 to 40 °C. The rate is presented by the Arrhenius type (exponential) of dependency of viscosity on temperature with the correlation coefficient R^2 > 99.9 % which indicates a good congruence with the Arrhenius plot. The Arrhenius equation modified for the case of viscous flow according to the sources [37, 38], is shown in (6),

$$\eta(T) = A_\eta . e^{\frac{E_\eta}{R.T}} ,$$ (6)

where $\eta(T)$ is a viscous flow, A_η is a constant, E_η is the activation energy for flow in [J/mol], R is the gas constant = 8.314 [J/mol.K] and T is the absolute temperature in [K].

Knowing a value of the exponent from the plot in Fig. 5.9, the activation energy of viscous flow can be calculated (7).

$$\exp = \frac{E_\eta}{R.T} \Rightarrow E_\eta = \exp .R.T$$ (7)

Viscosity measurements showed that despite relatively high solid loading, the 57 vol% dispersion embodies good flow behaviour both at lower (10 °C) and higher (40 °C) temperatures. It was proved that viscosity of the dispersion is mainly dependent on the viscosity of the monomers mixture and that particles influence the dispersion viscosity only slightly. This might show an evidence of a good stability of the particles within the dispersion. In discussion with [32], the 57 vol% dispersion should be suitable both for casting and also for using in stereolithography applications.

5.1.2.4   Photoinitiators addition

Three types of photoinitiators were studied and their influence on relative densities after sintering and average grain sizes was compared. Fig. 5.11 presents a comparison of different types of photoinitiators in respect to relative densities after sintering and average grain sizes. For this experiment were used three samples with exactly the same processing history so that they differed only in a type of photoinitiator.
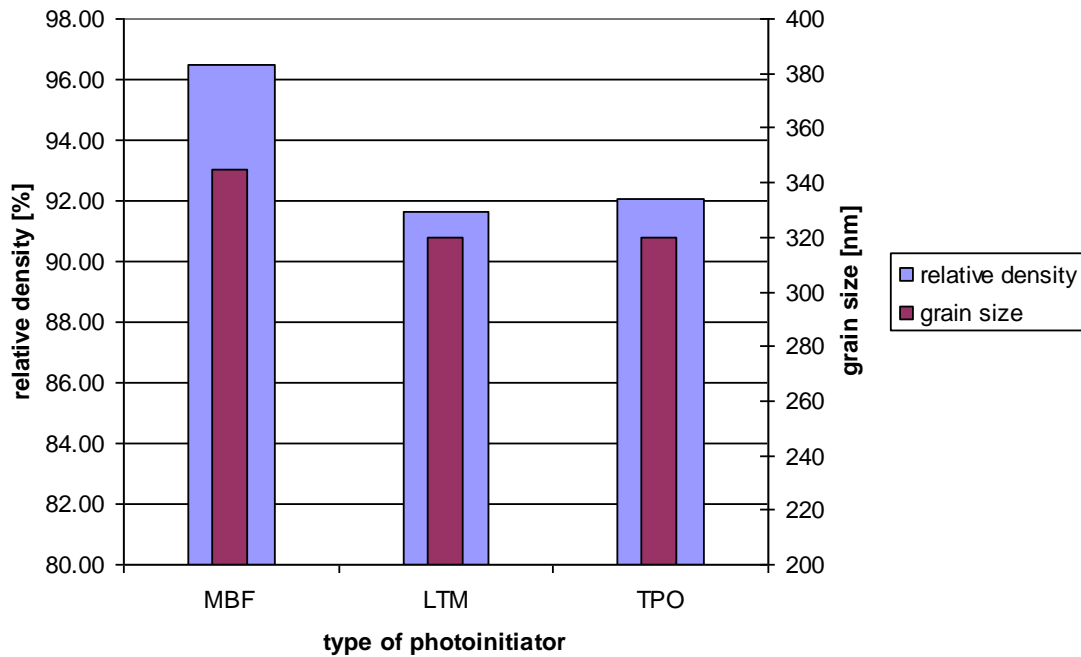
Fig. 5.11 Comparison of different photoinitiators in respect to the relative densities after sintering and average grain sizes.

The best ratio between relative density after sintering and average grain size was found for MBF photoinitiator. This initiator is totally organic which means that all the organic components can be burnt out leaving no residue. On the basis of this experiment, MBF photoinitiator was used for further processing.

5.1.2.5 Degassing of suspensions

After mixing the photoinitiator within the suspension a lot of air bubbles are trapped in the suspension. These bubbles can cause a creation of holes in cast layers which is unacceptable for further processing. Therefore, these bubbles had to be eliminated before casting, planarization and curing. Two types of bubbles removal techniques were examined in this work. At first degassing using vacuum pump was applied for LTM and MBF photoinitiator. In the case of LTM photoinitiator this technique worked well, however, it was realized that MBF photoinitiator evaporates quickly under lowered pressure. In order to use organic MBF photoinitiator, another approach for bubbles removal had to be applied. Suspensions were cast through a 180 μm mesh screen prior to planarization. This procedure will be called "sieving" in this thesis. This technique effectively removed entrapped air bubbles and improved the quality of cast sheets. As a result, higher relative density after debinding was achieved (Fig. 5.12).
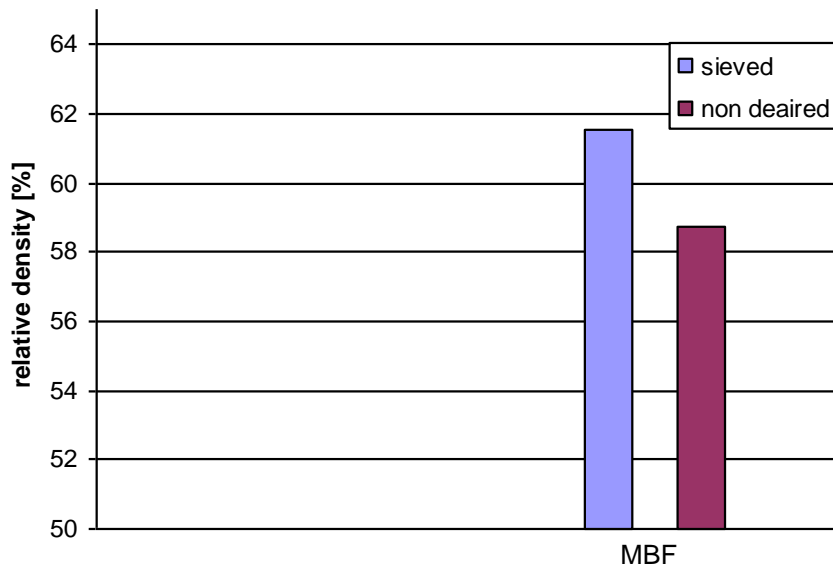
Fig. 5.12   Influence of sieving on density after debinding.

5.2   Powder washing

After measuring relative density of sintered bodies with Archimedes method, an inter-
esting question came up. Samples which were subjected to the Archimedes measure-
ment after debinding (to find out a relative density after debinding) showed after sinter-
ing consistently higher relative densities compared to non measured samples. This phe-
nomenon had to be investigated more closely. Therefore, it was assumed that some im-
purities which were not separated during centrifugation (e.g. Na) were responsible for
forming some chemical compounds which would somehow inhibit the sintering process.
On the basis of this assumption the stabilized powder (after centrifugation and drying)
was subjected to the TGA and compared to the TGA of the stabilized powder which was
re-dispersed (washed) in DIW and centrifuged one more time. The results of these
analyses are plotted in Fig. 5.13.
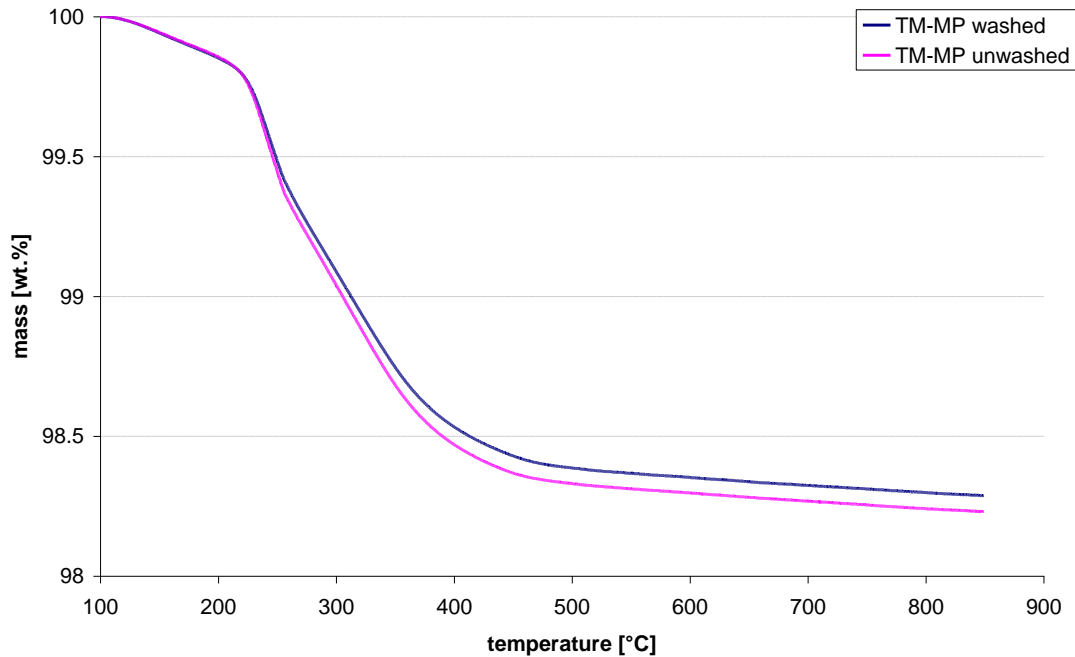
Fig. 5.13   TGA of washed and unwashed stabilized TM-DAR powder with adsorbed Melpers surfactants.

On the basis of the TGA was found that washing and second centrifugation removed even a bit more organic material from stabilized powder. This might be explained by even more profound separation of non adsorbed surfactants along with Na counter ions during second centrifugation. Nevertheless, several processing steps were improved when powder washing was applied.

- Very narrow PSD of re-dispersed powder in the monomers mixture was achieved already after planetary milling so that no ultrasonication had to be applied.

- Higher relative densities at debinded and sintered samples were achieved.

- Smaller grain sizes after sintering were acquired.

Comparisons between washed powder and non washed one will be made in further chapters.

5.3   Shaping

Three different kinds of shaping were studied in this work. The biggest attention was devoted to multilayer processing as a way of preparing transparent 1 mm thick alumina sheets through UV curing technique. As a side study, also extrusion and curing of thin fibers as well as curing of high definition microstructures using maskless lithography were studied.

5.3.1 Layering

Because of limited penetration of UV light through the material, the optimal thickness of layers warranting complete curing throughout the layer had to be found. Therefore curing depth of our suspensions was examined. Some authors have already studied the cured depth for UV curable systems containing 50 vol% of alumina powders [39, 40]. However, exact comparison of UV curing depth is not possible since the surfactants, resins, photoinitiators and powders (e,g, particle size) used in these studies are not similar to the ones used here. For alumina powders, sufficient depths were obtained at around 300 μm. The curing depth is strongly dependent on a refractive index contrast of the ceramic powder and the monomers. The higher is the difference in refractive indexes between monomers and powder the higher scattering appears and then smaller thickness can be cured [32].

In this work, monolayer and multilayer casting was performed. At first, 1 mm thick layer was cast and cured from both sides to verify the statements claimed in [39, 40]. However, the quality of the interior of these samples was not very good and in special cases it resulted even in a spongy/uncured interior. Hence, multilayer casting with a thickness of the layer of 250 μm was applied. Piling up of four layers by 250 μm finally formed a 1 mm thick multilayer sheet as showed in Fig. 5.14. Each layer was cured separately for 2 minutes. Layers were cast between two plastic foils using plastic stripes with a thickness of 250 μm as spacers.

Fig. 5.14   1 mm thick UV cured sheet comprised of 4 layers.

The effect of surface structure of foils on the surface of cast layers was observed. Fig. 5.15 shows the structures of two types of foils.
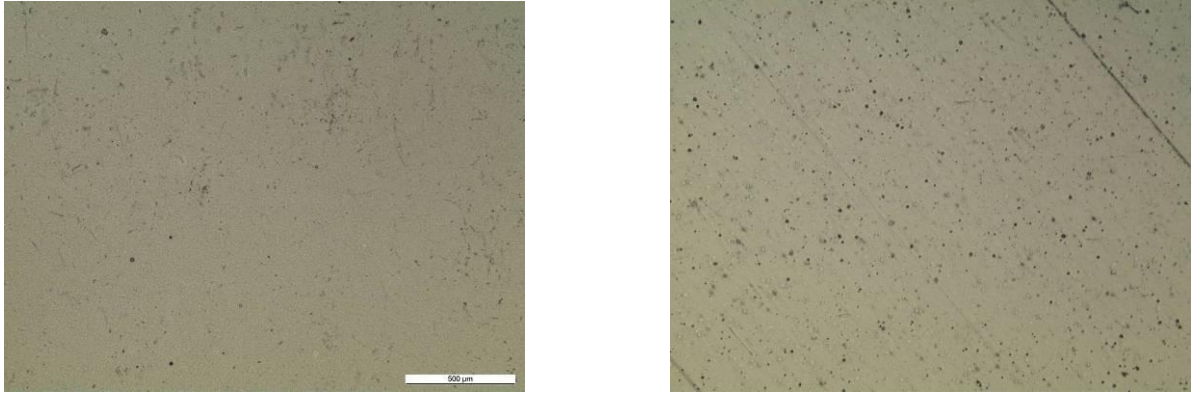
Fig. 5.15   Surface structure of two different foils (50x zoom): left - 3M™ foil for printing, right - PP foil.

PP foil embodied higher surface roughness which was finally printed to the cured (green) bodies as presented in Fig. 5.16 - right. The effect of surface relief was not so significant when 3M™ foil for printing was used (Fig. 5.16 - left).
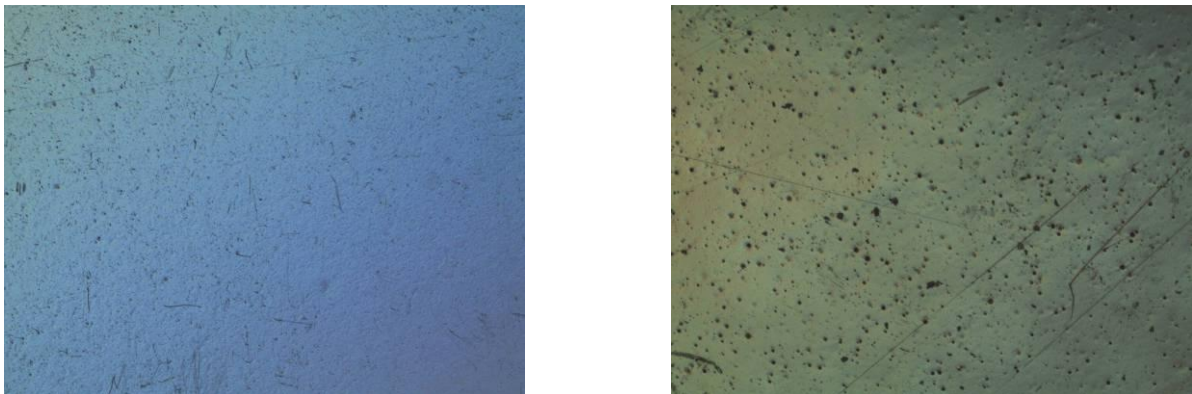
Fig. 5.16   Surface structure of cured body cast between: left - two 3M™ foils, right - two PP foils (50x zoom).

The surface quality is important especially because of a provision of a good adhesion between two layers, and the development of scattering centres for transparent ceramics. If the adhesion between two connected layers is not sufficient, delamination can occur during further processing (debinding). The effect of foil on layer roughness was discovered towards the end of the work when there was little time to seek improvements.

Furthermore, the effect of multilayer structure on relative densities after debinding and sintering was studied and described in chapters 5.4.1 and 5.5.

5.3.2   Fiber extrusion and maskless lithography

Fibers extrusion and maskless lithography shaping were carried out to demonstrate a versatility of shaping process with UV curable suspensions. Fibers were extruded and immediately cured in water as depicted in Fig. 5.17 [41]. Fibers longer than 0.5 m with 300 μm in diameter were successfully prepared.
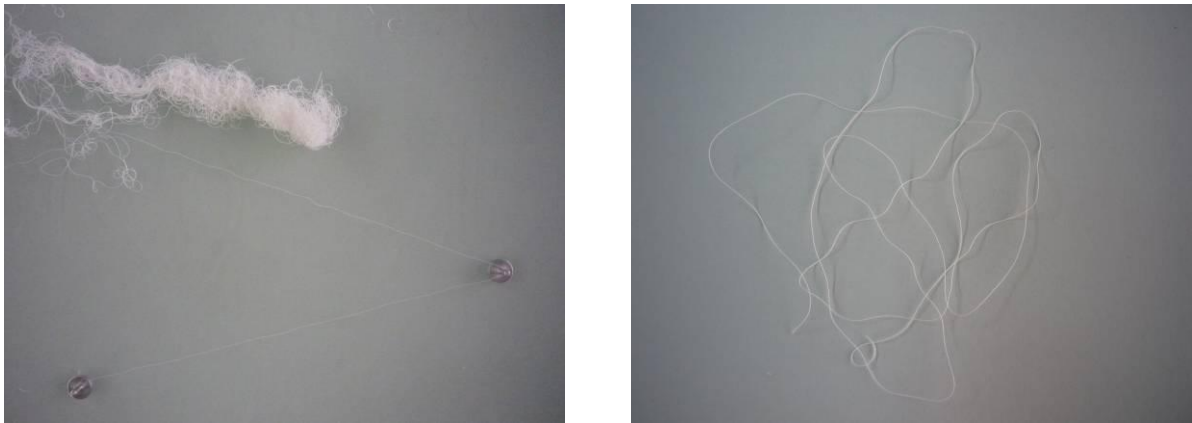
Fig. 5.17   Fibers prepared by extrusion and subsequent UV curing in aqueous medium.

High definition microstructures with a thickness of 100 μm and a resolution of less than cca 50 - 100 μm (aspect ratio = ~1-2) were cured using maskless lithography. These experiments give an evidence of a possible use of UV curable suspensions in shaping of high resolution structures such as patterns, various micro-scale nets and so on. Fig. 5.18 gives an example of such microstructures.
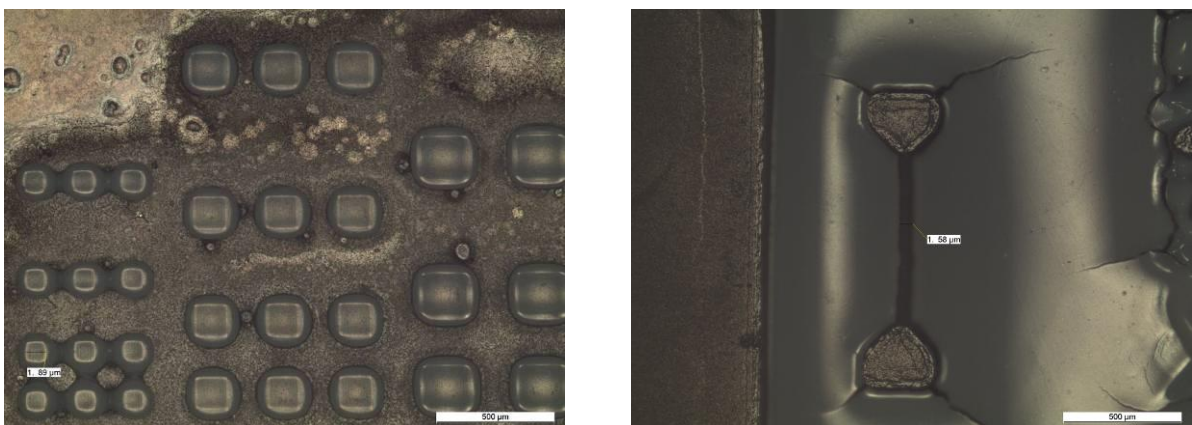
Fig. 5.18   High resolution structures prepared by maskless lithography (50x zoom).

5.4 Debinding

Debinding or organic binder burnout can be considered as a critical step in the whole processing involving solvent free dispersions. At this step an organic part is being removed from a component causing shrinkage of the component. The shrinkage can evolve a rise of cracks or delamination. The higher is the content of organic part the higher the shrinkage after debinding can occur. For the 53 vol% real solid loading (57 vol% of nominal solid loading) the rest that is 47 vol%, represents an organic part which is burnt out during debinding. Therefore a maximum theoretical linear shrinkage can be calculated provided that the shrinkage is uniform in the whole volume. Then the maximum linear shrinkage is $\sqrt[3]{47} = 3.61$ %. This theoretical presumption was verified by dilatometry measurements. At the same time, also an influence of different heating rates during dilatometry measurements on shrinkage was studied. Hence, two heating rates, 0.5 and 5 °C/min, were chosen for these measurements with the maximum temperature of 750 °C. The plots are demonstrated in Fig. 5.19.
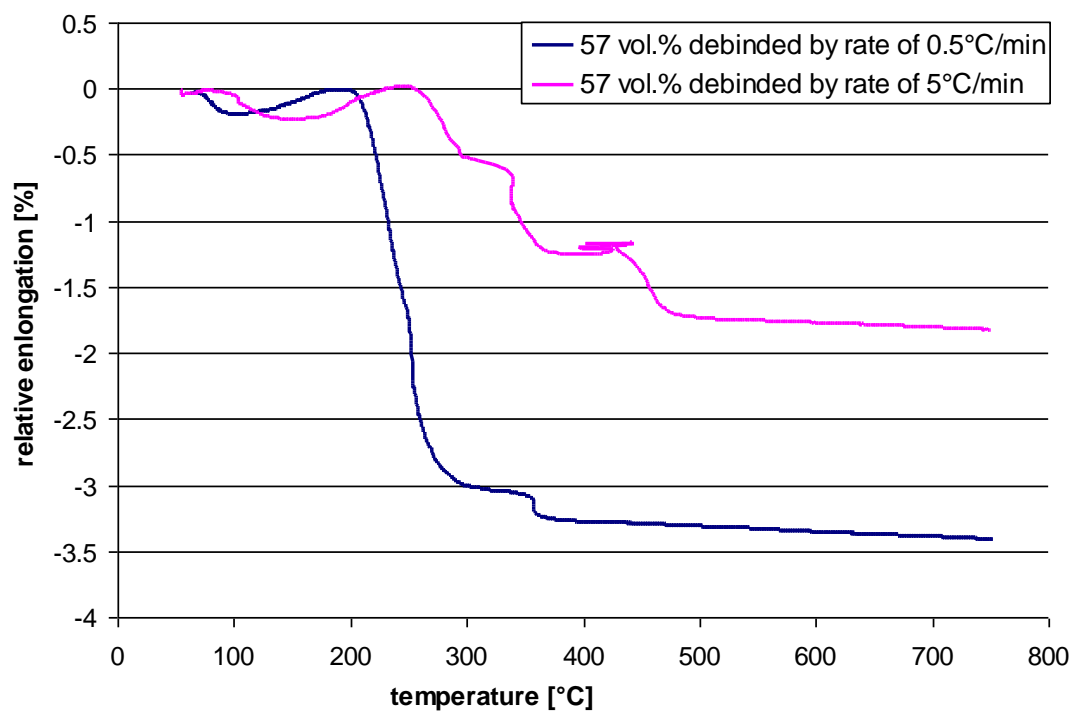
Fig. 5.19   Dilatometry measurements of the 57 vol% solid loading at different heating rates.

As one can see from Fig. 5.19, the heating rate significantly influences the shrinkage during debinding. While at a heating rate of 0.5 °C/min the shrinkage gets closer to the computed theoretical limit, at a heating rate of 5 °C/min the shrinkage stays far away from the theoretical limit. This could be explained by an aggressive developing of big pores substituting rapidly burnt organic material in the interparticle spaces. On the con-

trary, at very slow heating rates such as 0.5 °C/min, the burnout is slow and the pressure of releasing organic fumes does not reach as high values as in the case of faster heating rate. Therefore, the shrinkage should be homogeneous with creation of small pore sizes resulting in compact body after debinding. In order to demonstrate directly the influence of heating rate on organic burnout, TGA of 57 vol% solid loading cured bodies at two different heating rates was performed. The heating rates were 1 and 5 °C/min. The curves obtained from the TGA are shown in Fig. 5.20.
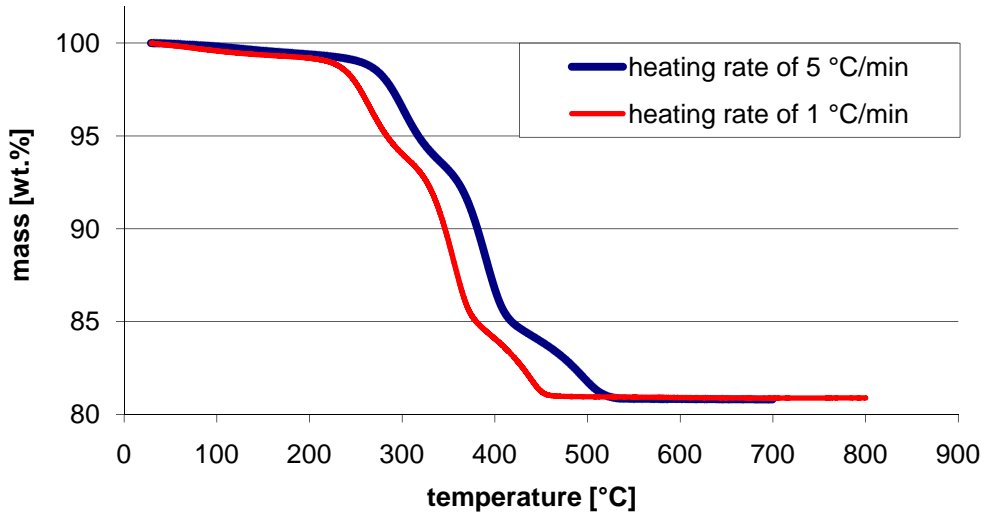
Fig. 5.20　TGA of 57 vol% solid loading with different heating rates.

From the curves in Fig. 5.20 is clear that at a faster heating rate the organic burnout takes place at higher temperatures. According to the ideal gas law (8),

$$p.V = n.R.T \, ,\tag{8}$$

where p is the absolute pressure of the gas [Pa], V is the volume of the gas [m^3], n is the amount of substance [mol], R is the gas constant and T is the absolute temperature [K], the pressure and/or volume have to be increased when temperature is increased. This might cause a particle re-arrangement which hinders subsequent shrinkage. As a result, cracked or very fragile samples were obtained after debinding at 5 °C/min. The TGA depicted in Fig. 5.20 also gives information about the maximum temperature at which the last organic material is burnt out. Therefore, based on the TGA and dilatometry measurements, the debinding temperature of 650 °C and the heating rate of 0.5 °C/min were finally selected for debinding procedure.

Although the selected debinding regime seems to be very slow, in bulky components where the heat transfer from the surface into the core of the component is delayed, some internal pressures or stress tensions can be induced. Hence, in effort to control the

debinding process even more effectively in respect to the bulky components, and to eliminate these strains, it might have been favourable to use a cascade heating regime with dwell times at critical temperatures where burning of the specific organic part takes place. On the basis of the differential thermal analysis (DTA) is possible to determine at which temperatures a burnout of a certain organic part takes place. The DTA and TGA of the 57 vol% solid loading cured body are shown in Fig. 5.21.
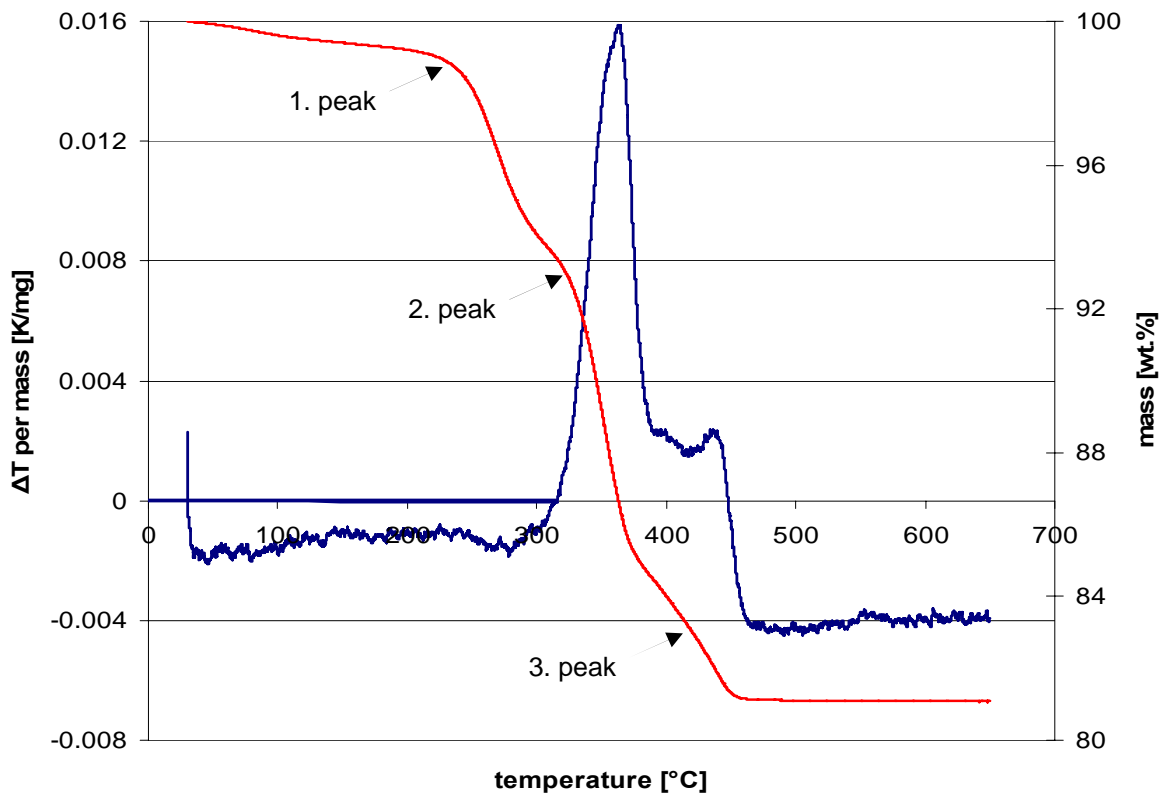
Fig. 5.21   DTA and TGA of 57 vol% solid loading cured body at a heating rate of 1°C/min.

DTA revealed that an exothermal reaction occurred at a temperature range of cca 320 and 450 °C. At this temperature range a main burnout of organic part is therefore expected which also corresponds with TGA curve where the temperature of 320 °C indicates a place where the second peak on TGA curve appears. In order to study the influence of dwell time on mass loss during isothermal debinding, another TGA was carried out for 57 vol% solid loading cured bodies at a heating rate of 1°C/min with dwell times of 4 hours at different temperatures. The results of this experiment are demonstrated in Fig. 5.22.
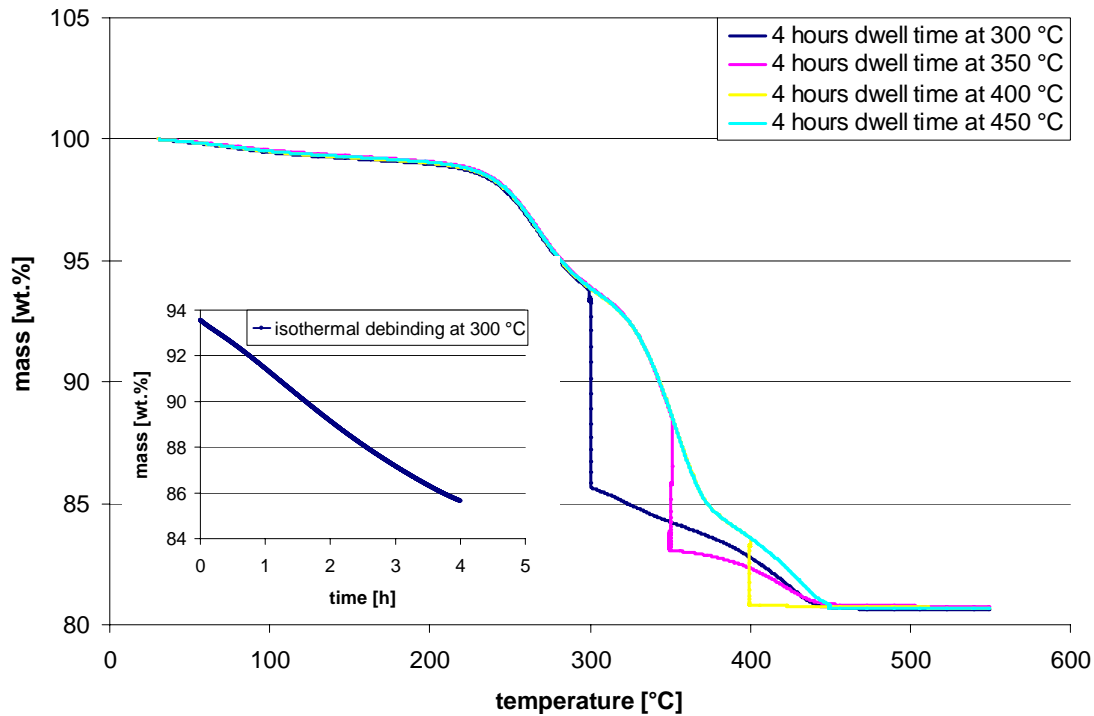
Fig. 5.22   TGA of 57 vol% solid loading cured bodies at a heating rate of 1°C/min with dwell times at
           different temperatures.

The TGA depicted in Fig. 5.22 revealed that isothermal debinding allows burnout at lower temperatures. It was also found that when the temperature which corresponds to the beginning of the second peak on TGA curve was chosen as an isothermal debinding temperature, the burnout proceeded almost till the beginning of the third peak. It is assumed that with longer dwell time at 300 °C the burnout would finish even closer to the beginning of the third peak. This might indicate a possibility of isothermal debinding from peak to peak which should result in reduced stresses inside the bulky components. However, further investigation in this direction would be beyond the frame of this thesis.

5.4.1   Relative densities after debinding

High relative densities after debinding are desirable in production of compact and highly homogeneous structures. Such densities can be obtained only by uniform packing of the ceramic particles within the debinded body. In order to approach to this stage, however, the highest possible solid loading has to be used. On the basis of this assumption, in this work, also the highest possible solid loading which allows convenient shaping was found and further worked with. The bar chart in Fig. 5.23 shows a development of relative densities after debinding in our processing.
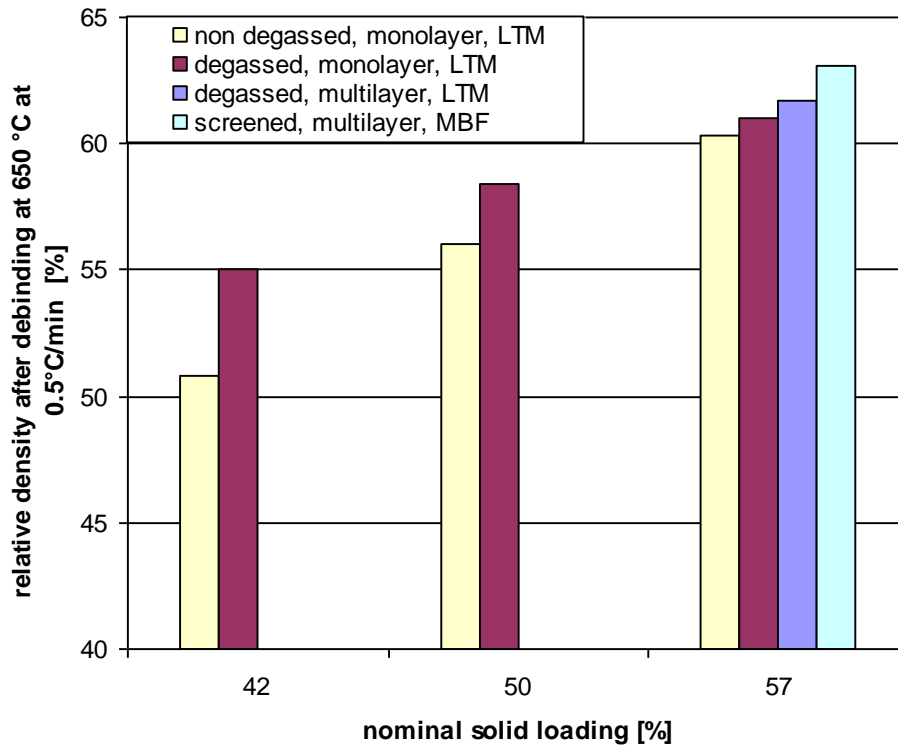
Fig. 5.23   Development of increasing relative densities after debinding.

As discussed previously, it was discovered that degassing (bubbles removal) had a significant effect on increase in relative densities after debinding. However, the effect was smaller with increasing solid loading. Relative density after debinding also grew with higher solid loading which was expected. On the other hand, the viscosity also rose with increasing solid loading which was confirmed in Fig. 5.7. Hence, for very high solids loading, the problems with re-dispersing of the ceramic powder in the monomers mixture began to occur. Therefore, in this work, the limit value of solid loading was found to be around 57 vol%. Furthermore, it was found that multilayer structures were reaching higher relative densities after debinding then monolayer ones (see Fig. 5.24 below), and finally, using MBF photoinitiator instead of LTM also improved the relative density after debinding. As a result of all the optimizations, debinded bodies with relative densities of more than 63 % were finally achieved.

5.5   Sintering

Sintering was performed with a view to reach closed porosity and as small grain sizes as possible. Closed porosity is necessary for further HIP operation as explained in chapter 3.8, and very small grain sizes are important from a transmittance behaviour point of view as discussed in chapter 3.5.1. Therefore several one-step sintering regimes and shortly also pre-sintering heat treatment and two-step sintering were explored and their

influence on grain sizes and relative densities was studied. In discussion with [42, 43], first sintering regimes were suggested. In these works [42, 43] also sintering of alumina powder was carried out. The structure of sintered samples was observed with scanning electron microscope and average grain sizes were measured. Relative density was measured using Archimedes method. All here presented measurements were performed with samples debinded at a final temperature of 650 °C at a heating rate of 0.5 °C/min. The standard dwell time at maximum temperature at single-step sintering was set to 6 hours as suggested in [42]. The standard heating and cooling rate for sintering was set to 10 °C/min. In the following table - Table 2, sintering temperatures, dwell times and heating rates used for sintering of samples with different processing history are presented.

Table 2
Overview of sintering regimes and a composition of samples subjected to sintering.

Sintering temperature [°C]	Dwell time [h]	Heating rate [°C/min]	Solid loading [vol%]	Degassing/ sieving/ - [D/S/-]	Photoin. [LTM/MBF]	Layering [Y/N]*	Solvent addition [Y/N]*	Powder washing [Y/N]*
1325	6	10	57	S	MBF	Y	Y	Y/N
1350	6	10	42 50 57	D/- D/- D/S/-	LTM LTM LTM/MBF/LTM	Y/N	N N N/Y/N	N N N/Y/N
	9	10	57	S	MBF	Y	Y	Y/N
1375	6	10	57	S	MBF	Y	N	N
1400	6	10	57	S	LTM MBF	Y	N	N
1450	6	10	42 50 57	D/-	LTM	Y/N	N	N

*Y/N means YES and/or NO

In the following, comparisons of different aspects in respect to the relative densities after sintering and average grain sizes are given. At first the influence of solid loading, degassing and multilayer casting on density after sintering at 1350 °C for 6 hours was studied and is depicted in Fig. 5.24.
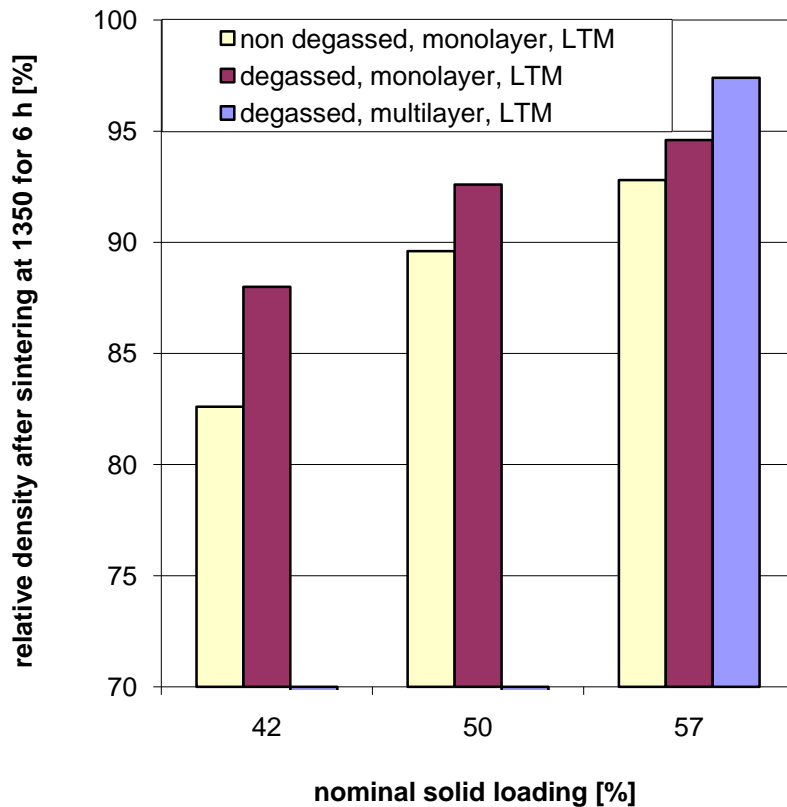
Fig. 5.24   Influence of solid loading, degassing and layering on relative densities after sintering.

In all cases of solids loading was proved that degassing improved density after sintering. The decreasing difference in relative densities between degassed and non degassed suspensions with increasing solid loading can be explained by raising viscosity and so increasing difficulty in bubbles releasing. It is also evident that multilayer casting increased relative density after sintering. On the basis of these results, 57 vol% suspension was further selected and used for other experiments. The influence of the photoinitiator, Archimedes measurement of debinded bodies (the influence of Archimedes measurement will be called in further text as washing prior to sintering) and powder washing (this powder washing will be called in further text as washed and re-centrifuged powder) on relative density after debinding was studied. Fig. 5.25 shows a development of relative densities after sintering at samples with different processing history.
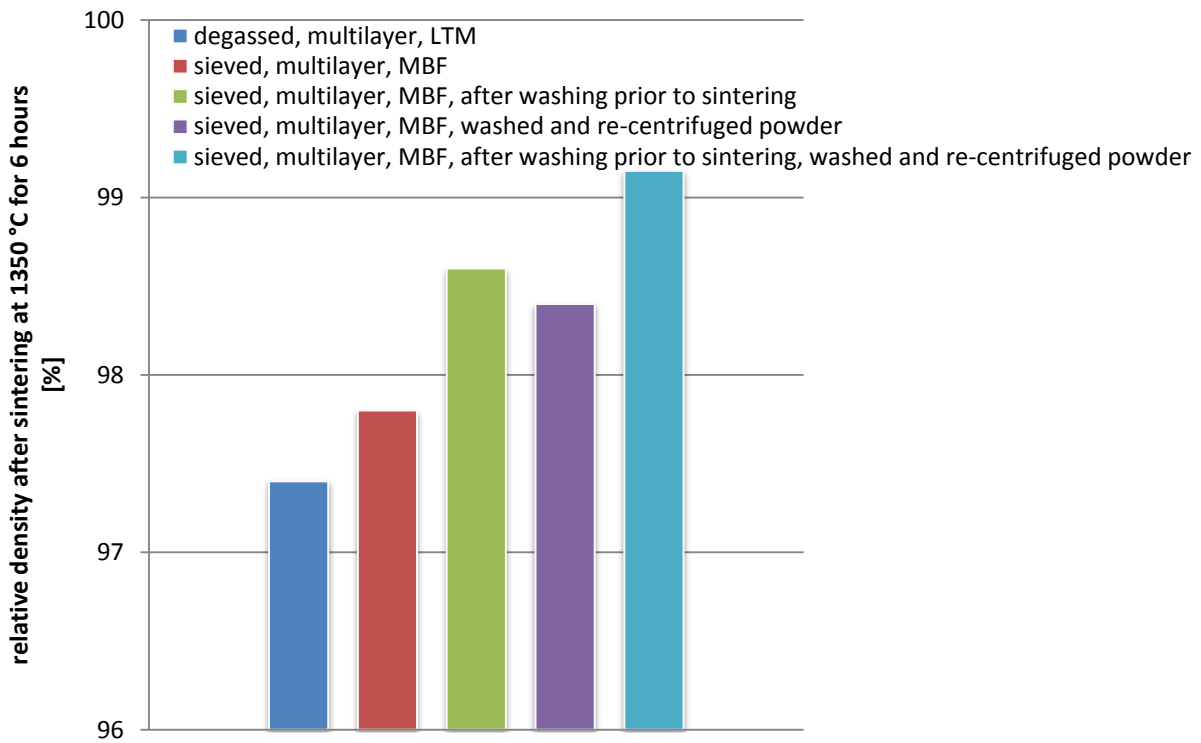
Fig. 5.25   Development of relative densities after sintering.

It was found that washed and re-centrifuged powder along with the influence of sample washing prior to sintering increased relative density after sintering. These influences were further studied and particular contributions to final densities from these procedures were calculated and presented in Table 3. This table contains data for samples with 57 vol% solid loadings, with MBF photoinitiator, after sieving, with multilayer structure, and after debinding at 650°C by heating rate of 0.5°C/min.

Table 3
Influence of washed and re-centrifuged powder and washing prior to sintering on relative densities after sintering.

Procedures	Relative density after sintering at 1350 °C for 6 h
non washed and re-centrifuged powder, no washing prior to sintering	97.21 %
washed and re-centrifuged powder, no washing prior to sintering	98.43 %
non washed and re-centrifuged powder, washing prior to sintering	98.50 %
washed and re-centrifuged powder, washing prior to sintering	99.16 %

From Table 3 implies that a difference in relative densities between non washed and re-centrifuged powder powder with no washing prior to sintering and washed and re-centrifuged powder with washing prior to sintering is almost 2 %. At the same time, it is evident that contributions for increase of relative density are almost equal for both washed and re-centrifuged powder and washing prior to sintering and correspond to cca. 62.6 % respectively 66.2 % of the total increase of relative density. If both procedures are applied the increase in relative density from washing prior to sintering is reduced to cca. 37.4 %. The principle of increasing density after either washed and re-centrifuged powder or washing prior to sintering, however, is not clear. There can be two possible explanations of this phenomenon. Firstly, the increase in density is caused by washing out the impurities which somehow hinder the sintering process and secondly, this increase can be contributed by particle re-arrangement during washing prior to sintering. Also a combination of both is possible. However, when relative densities of washed and re-centrifuged powder with no washing prior to sintering (rel. dens. 98.43 %) and non washed and re-centrifuged powder with washing prior to sintering (rel. dens. 98.50 %) are taken into an account, it is evident that washing and re-centrifuging powder, which means removing the impurities, is effective in respect to increase of relative density after sintering. It is also not at all readily understood why particle rearrangement during such non-controlled washing and drying procedure would always result in a favourable particle rearrangement configuration for sintering.

5.5.1   Sintering temperature, relative densities and microstructure

Table 2 described applied sintering regimes. In this chapter are presented results of chosen sintering regimes in terms of achieved relative densities and microstructure (grain sizes). Table 4 summarises achieved relative densities and grain sizes for various sintering regimes and washing procedures.

Table 4
Achieved relative densities and grain sizes for various sintering regimes and washing procedures.

Sintering regime	Washed and re-centrifuged powder [Y/N]	Washing prior to sintering [Y/N]	Relative density [%]	Average grain size [nm]
1350 °C / 6 h	Y	Y	99.1	270
1375 °C / 6 h	N	N	98.3	300
1400 °C / 6 h	N	Y	98.8	410
1450 °C / 6 h	N	N	96.5	800

Figs. 5.26-5.29 show microstructures of samples sintered at different temperatures. Unless mentioned, all the pictures in Figs. 5.26-5.29 describe a surface of sintered sheets.
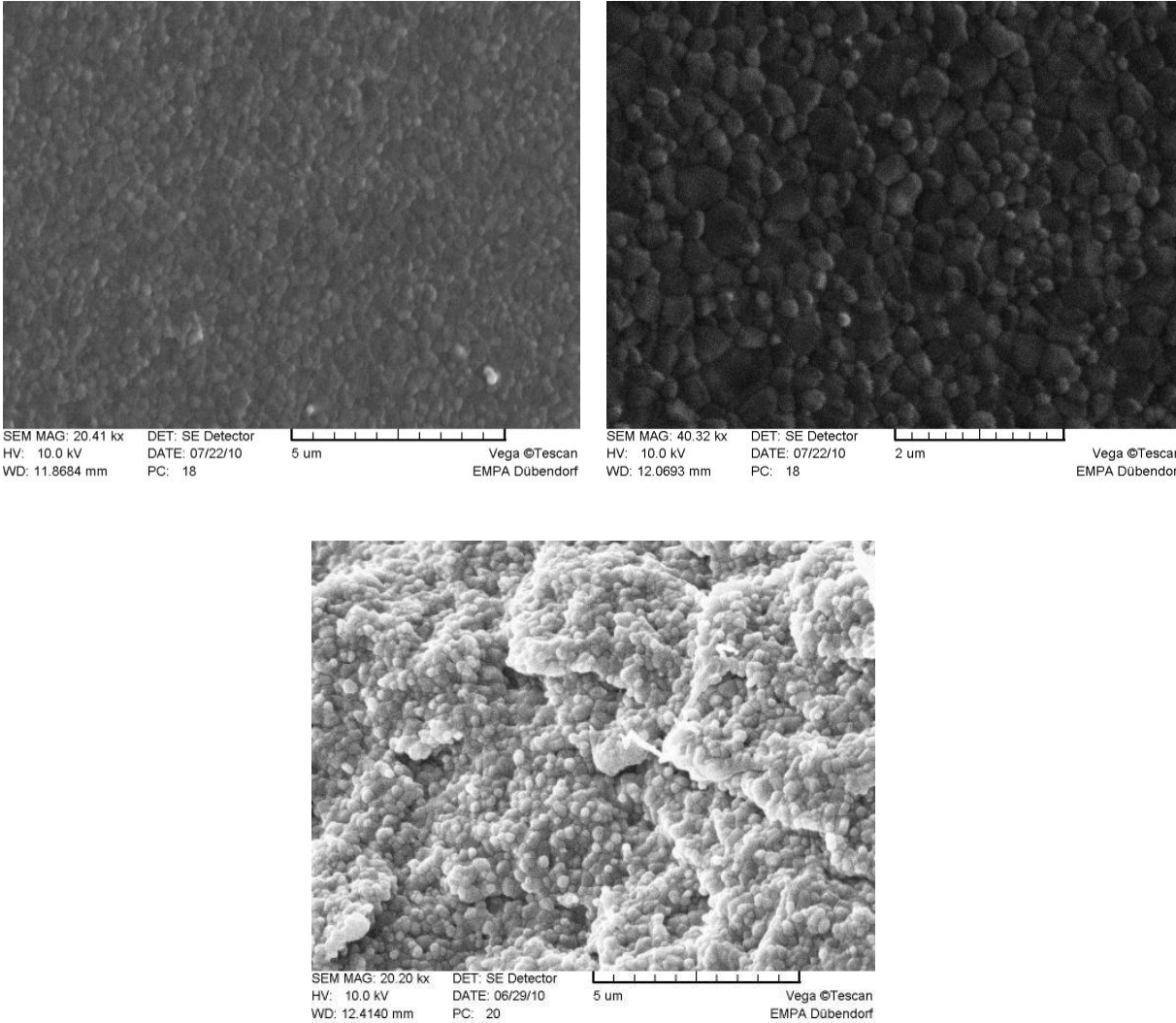
Fig. 5.26   Microstructure of a sample sintered at 1350°C for 6 hours (left cca. 20,000x zoom, right cca. 40,000 zoom, middle - fracture section, cca. 20,000x zoom).
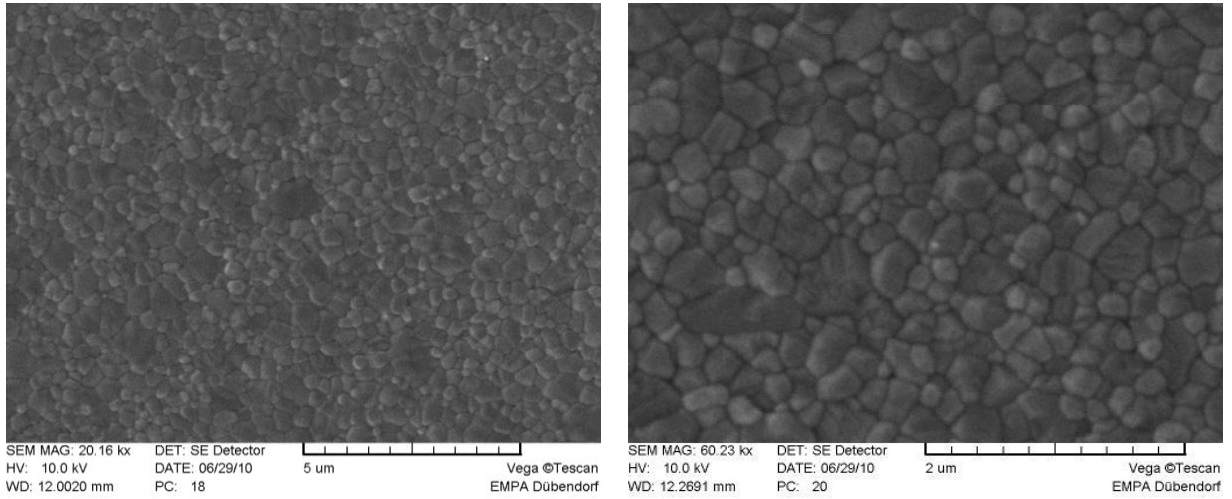
Fig. 5.27   Microstructure of a sample sintered at 1375°C for 6 hours (left cca. 20,000x zoom, right cca. 60,000x zoom).
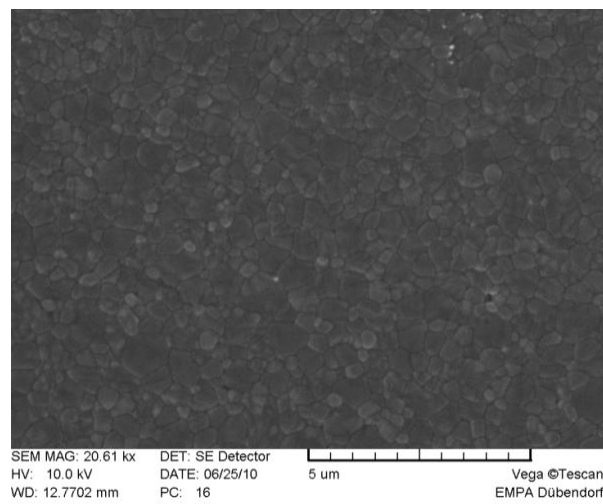
Fig. 5.28   Microstructure of a sample sintered at 1400°C for 6 hours (cca. 20,000x zoom).
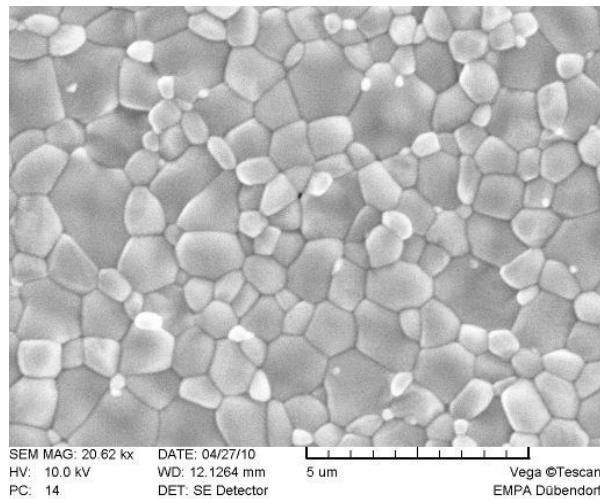
Fig. 5.29   Microstructure of a sample sintered at 1450°C for 6 hours (cca. 20,000x zoom).

All the samples at which relative density after sintering exceeded 97.0 % were further subjected to final HIP operation. 97.0 % relative density is considered to be sufficient to assure completely reduced opened porosity within a sample.

5.5.2   Pre-coarsening and two-step sintering

Pre-coarsening step as a pre-sintering heat treatment at lower temperatures to decrease residual porosity after sintering was successfully applied at MgO doped alumina [44]. In this thesis also pre-coarsening step was shortly studied, however any effect on grain size reduction was observed which is in agreement with findings presented in [44] for pure alumina.

Two-step sintering was also shortly examined in this thesis, however with similar results as the pre-coarsening treatment. No significant improvement in microstructure was observed compared to single step sintering which is in accord with results announced in [45].

5.6   Solvent addition

In order to make an interlink between non aqueous UV curing and traditional aqueous gel casting, at first ethanol and then DIW were added to ceramic suspension. This combination could link up advantages and partially reduce disadvantages of both techniques. At gel casting the gelled body contains a big amount of water so that drying is a critical step because of high shrinkage during water evaporation. At UV curing the cured

body contains a big amount of organic compounds so that debinding is a critical step because of high shrinkage caused by burning out of organic part. The motivation for making this experiment was following:

- improved fluidity of ceramic suspension
- separation of shrinking process into two stages – drying and debinding

At first, 30 vol% of the monomer mixture was substituted by 30 vol% of ethanol. Incurred mixture was unstable because of fast evaporation of ethanol which led to very high solid loading and loss of fluidity. Therefore, this mixture was left for one day on air to let ethanol be completely evaporated. After that the solidified slurry was successfully re-dispersed in DIW, at first at 30 vol% of DIW substituting 30 vol% of the monomer mixture and subsequently was prepared also a suspension with 15 vol% of DIW substituting 15 vol% of the monomer mixture. These suspensions were cast and UV cured as monolayer and multilayer structures and further dried. Fig. 5.30 shows these structures.

a) b)

Fig. 5.30   UV cured multilayer (left) and monolayer (right) sheets of the suspensions with:
a) 15 vol% of DIW substituting 15 vol% of monomer mixture and
b) 30 vol% of DIW substituting 30 vol% of monomer mixture.

Significant bending appeared during drying period (at room temperature on air) at monolayer sheets, especially at the sheet with 30 vol% of DIW. Bending was not so considerable at multilayer structures. Eventually only very small bending appeared at the multilayer sheet with 15 vol% of DIW. Relative density of multilayer sheets was measured after debinding resulting in 63.1% for the suspension with 15 vol% DIW addition and 59.6 % for the suspension with 30 vol% DIW addition. While the samples with

30 vol% water addition were very fragile and were cracking when handling, samples with 15 vol% water addition were rather tough and did not crack when handling. No cracking of samples during debinding was observed. TGA was also performed at these suspensions and is presented in Fig. 5.31.
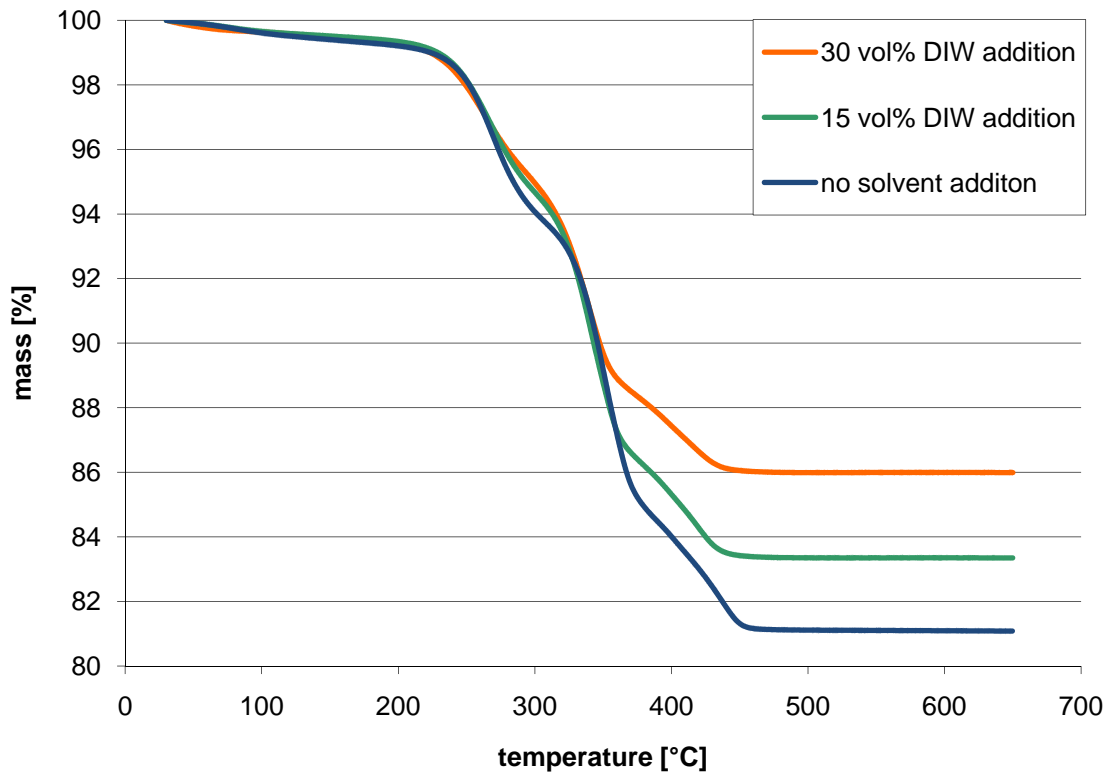
Fig. 5.31   TGA of 57 vol% suspensions with and without solvent (DIW) addition.

Mass loss at 15 and 30 vol% DIW addition suspensions corresponds to the amount of monomers which were substituted by water. It means that water was successfully removed from cured bodies by evaporation on air.

Sintering was performed at two temperatures, 1325 and 1350 °C for 6 hours. Table 5 describes achieved densities taking into account also the influence of washing prior to sintering.

Table 5
Relative densities after sintering of suspensions with addition of DIW.

Solvent addition	Sintering temperature	Washing prior to sintering	Relative density
15 vol%	1325 °C	YES	91.6 %
		NO	86.6 %
	1350 °C	YES	97.7 %
		NO	94.2 %

30 vol%	1325 °C	YES	87.4 %
		NO	80.4 %
	1350 °C	YES	N/A
		NO	N/A

It was found out that the addition of 15 vol% of water in UV curable suspension substituting the same volume of the monomers mixture could be used for next shaping and curing resulting in improved fluidity. However it seems that 15 vol% water addition is a limit because of bending during drying. Therefore less than 15 vol% water addition would be favourable to use. It is also recommended to repeat the experiment with direct dispersion in water/monomer mixture (without ethanol step).

5.7 Hot isostatic pressing

Two HIP regimes were used for suppressing of residual porosity after sintering. First HIP was performed at 1400 °C for 4 hours at 200 MPa. This HIP regime resulted in completely reduced porosity on one hand, however, as expected from the high temperature, in a very coarsened microstructure with grain sizes in order of micrometers on the other hand. Fig. 5.32 shows a surface structure of a sample sintered at 1350°C for 6 hours before and after HIPing.

a)   b)
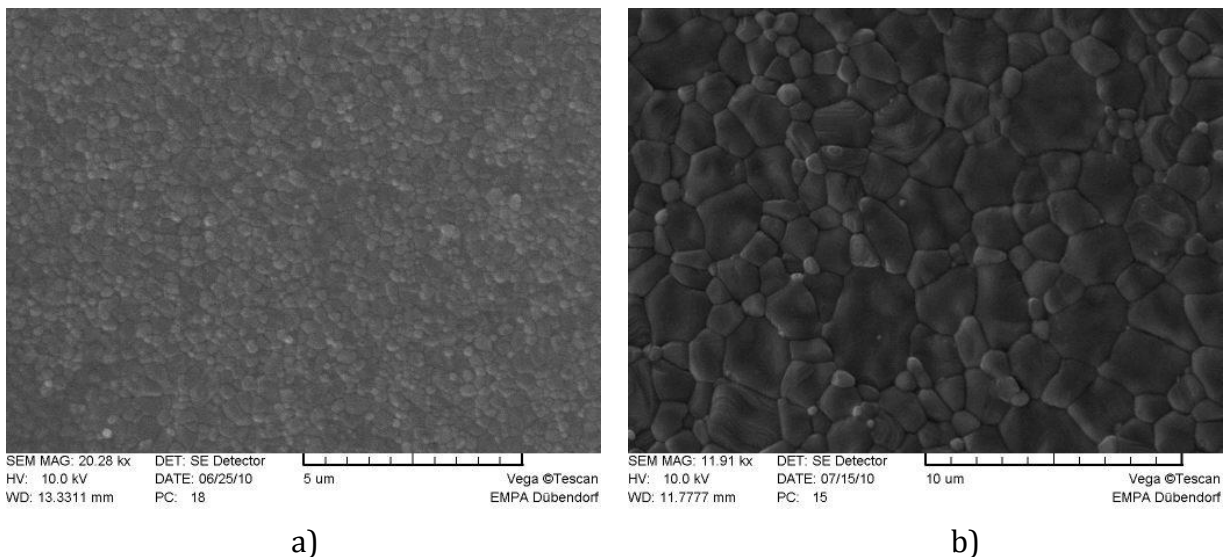
Fig. 5.32 Microstructure a) before and b) after HIP at 1400 °C for 4 hours at 200 MPa.

Despite very coarsened microstructure, some light transmission was observed at 0.5 mm thick sheets. Fig. 5.33 depicts two 0.5 mm thick sheets. The left dark sheet is

contaminated by carbon coming from carbon heating elements of a furnace for HIP. Several contaminated samples after HIP in this furnace were annealed at 1350 °C for several hours. As a result, most of the carbon diffused out of contaminated sheets, which is illustrated in Fig. 5.33 (right).
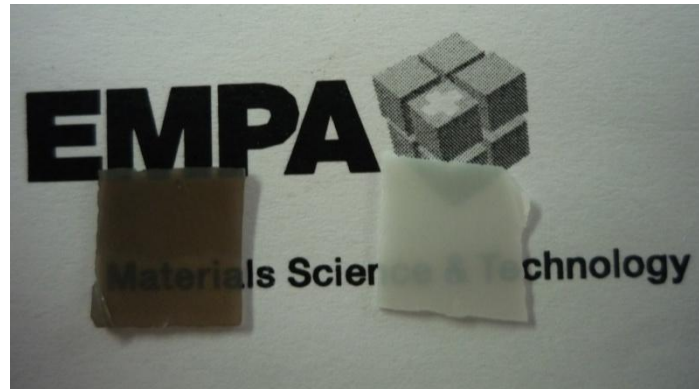
Fig. 5.33 0.5 mm thick sheets HIPed at 1400 °C for 4 hours at 200 MPa

Second used HIP regime was performed at 1200 °C for 2 hours at 198 MPa. These conditions were used for gel cast bodies. It was discovered, however, that these conditions were not sufficient for eliminating of residual porosity so that relative density did not reach 100 %. Also no grain growth was observed. Fig. 5.34 shows microstructures (surfaces) before and after HIP at 1200 °C for 2 hours at 198 MPa.
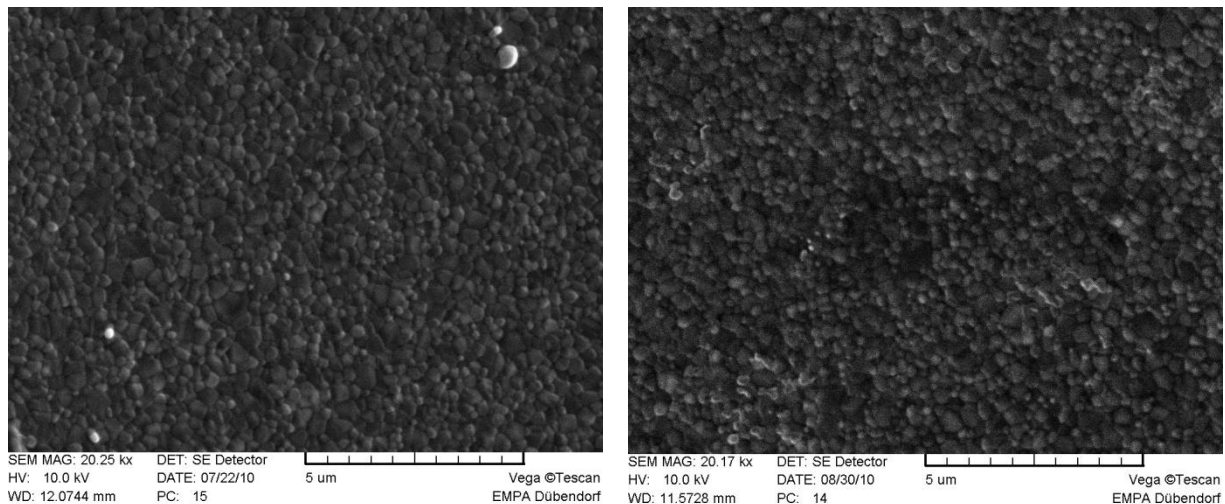
Fig. 5.34 Microstructure a) before and b) after HIP at 1200 °C for 2 hours at 198 MPa.

On the basis of these results it seems that the optimal HIP temperature should be found somewhere around 1275 and 1300 °C and optimal time at highest temperature is suggested to be between 2 and 4 hours.

5.8 Light transmission measurements

Transmission of the light through alumina sheets with thickness 0.45 and 0.9 mm was measured. At all measured samples washing prior to sintering was performed. However, only very low light transmission in visible spectrum (several %) was detected at 700 nm wavelength at thinner sheets. Fig. 5.35 illustrates light transmittance through alumina sheets in dependence on used wavelength after HIP at 1200 °C for 2 hours at 198 MPa.
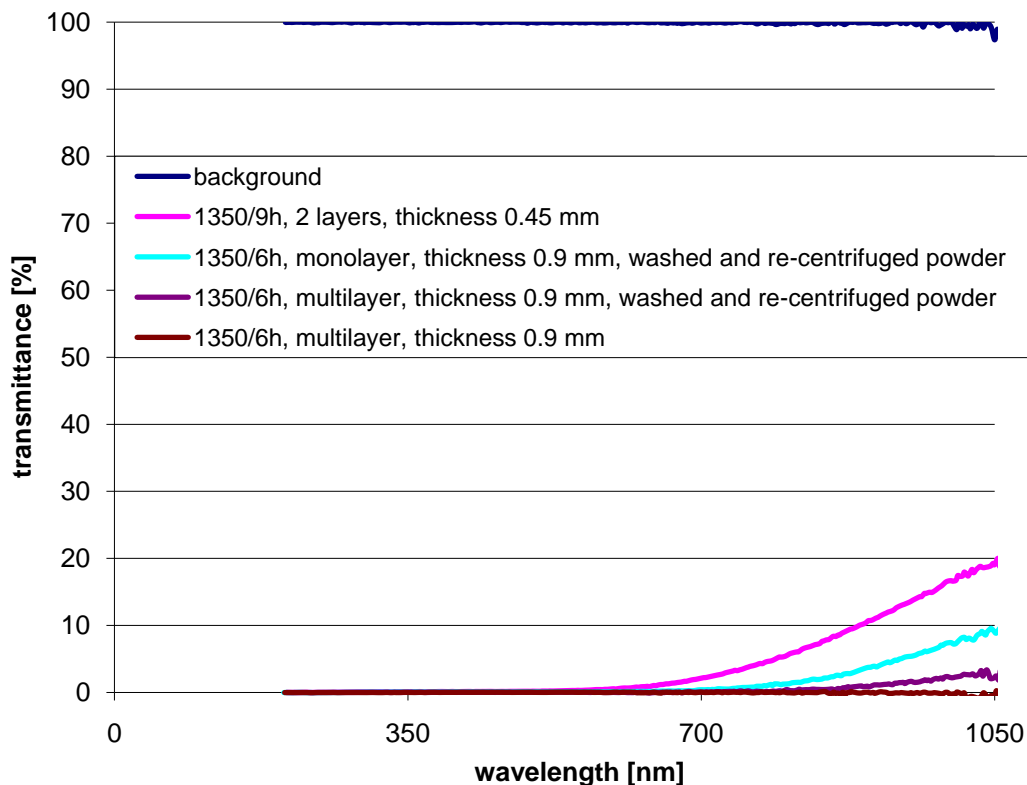
Fig. 5.35   Light transmission through alumina sheets with thickness 0.45 and 0.9 mm.

It is evident that light transmission through a sheet is higher with decreasing thickness of the sheet which is in a good agreement with Krell [1]. Moreover, multilayer structures, especially having rough surfaces, can also cause significant scattering of the light beams. This might be a reason why monolayer sheet transmits more light than multilayer sheets.

In IR spectrum the light transmittance increases because the wavelength becomes bigger than pore sizes and/or grains.

5.9 Hardness measurement

Hardness was measured after sintering and after HIP at samples with various relative densities and grain sizes. Hardness measured at sintered samples with relative density

of 99.1 % and average grain size of 270 nm was HV2 = 2235 (at testing load of 2 kgf). Standard deviation for all the measurements was 3.75 % at maximum. Hardness measured at samples after HIP at 1400 °C for 4 hours at 200 MPa with relative density of 100 % and with grain sizes within the range of several micrometers resulted in HV2 = 2210 and finally hardness measured at samples after HIP at 1200 °C for 2 hours at 198 MPa with non changed average grain size (270 nm) and relative density of 99.8 % was HV2 = 2310. In all cases hardness exceeded HV2 = 2200 which corresponds to HV2 > 21.5 GPa which confirms the statement presented by Krell [1], (see chapter 3.3).

5.10   High resolution microstructures

To demonstrate the range of attainable shapes using UV curing technique, some high resolution microstructures were made using maskless lithography. The time necessary for complete curing for LTM and MBF photoinitiators was studied. It was found that the time necessary for complete curing of ~100 micrometer thick films was 20 s in the case of MBF photoinitiator and 0.5 s in the case of LTM photoinitiator. This exposure time resulted in best resolution microstructures. Fig. 5.36 shows achieved microstructures.
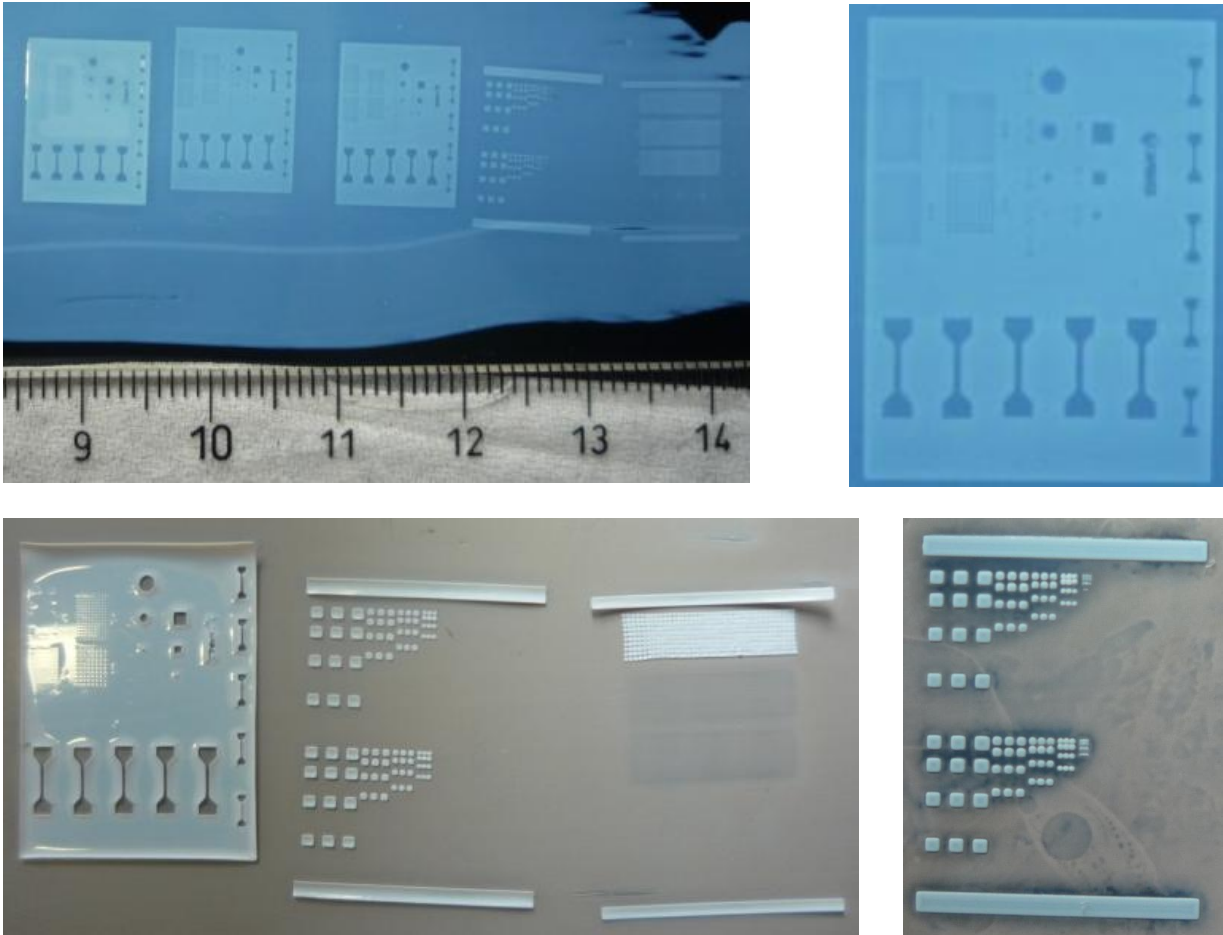
Fig. 5.36   Microstructures produced with maskless lithography.

5.11   Summary of results

In the following tables (Table 6a, 6b), a comparison of baseline variables or parameters with optimized or best parameters is made.

Table 6a

Comparison of baseline process variables with best achieved process parameters.

Process variable	baseline	optimization	best
Solid loading (nominal)	42 vol.%	√	57 vol.%
Photoinitiator	LTM	√	MBF
Layer thickness	1x1000 μm	√	4x250 μm
Debinding rate	0.9 °C/min	√	0.5 °C/min
Max. debinding temperature	650 °C	x	650 °C
Sintering temperature	1500 °C	√	1350 °C
Sintering dwell time	2 h	√	6 h
HIP temperature	-	x	x
HIP dwell time	-	x	x
Washing prior to sintering	-	√	√
Washed and re-centrifuged powder	-	√	√
Solvent addition	-	√	x

Table 6b

Comparison of baseline quality variables with best achieved quality parameters.

Quality variable	baseline	optimization	best
Vacuum degassing	-	√	x
Sieving	-	√	√
Substrate foil	polypropylene	√	3M™ printing foil

Alumina sheets prepared by UV curing technique did not reach as high level of transparency as expected. There are several reasons for this:

- Poor integrity of the sheets – at monolayer sheets, problems with complete curing appeared. At multilayer sheets interlayer decohesion or delamination appeared. It is concluded that plastic foils (respectively their surface roughness) used for planarization of the suspension during layer casting are suspected from poor interlayer adhesion, later causing delamination.

- Suitable HIP regime could not be applied. Therefore basic requirements for provision of transparency such as relative density 100 % and/or grain size lower than 500 nm could not be fulfilled.

On the other hand, it has to be highlighted here that not all the parameters studied could be implemented. Experiments with different foils or no substrate at all started late and there was not enough time for deeper investigation. Also addition of DIW to dispersions turned out to be promising and worth having for further investigations. Unfortunately there was no time to repeat experiment without previous step with addition of ethanol.

6.   Conclusions and outlook

The aim of this work was to prepare transparent ceramic sheets made out of sub-µm alumina powder through UV curing in UV curable resin. Because of limited penetration depth of UV light, layer by layer curing had to be applied. 1 mm thick sheets were produced comprised of 4 layers by 250 µm. Highly loaded sterically stabilized colloidal suspensions with real solids loading of 53 vol% were finally used for sheets production. These suspensions containing only ceramic powder and curable organic compounds were shaped in various ways, e.g. monolayer and multilayer sheets, fibers and high resolution monolayer microstructures. It is assumed that the possibility of curing layer by layer could enable making complicated multilayer 3D structures with resolution in order of less than 100 µm using stereolithography or robocasting. However, a big content of organic part in the suspensions caused problems with debinding. Therefore very slow debinding regime had to be used to prevent cracking or delamination during organic burnout. This process could be controlled even more thoroughly using sophisticated multistep debinding. A possibility of solvent addition to divide debinding step into drying and debinding was briefly studied using deionized water and ethanol. It is suggested that further investigation in this direction would reduce problems with debinding and, at the same time, could improve fluidity of suspensions. Problems with delamination occured, therefore it is supposed that using smoother substrate or no substrate at all (e.g. with stereolithography) should reduce the presence of delamination. Bubbles contained within the suspensions were effectively removed by either degassing or sieving in dependence on used photoinitiator. However, it might have been favourable to use totally organic photoinitiator which would not evaporate under lowered pressure. As a result of optimizations of suspension composition, multilayer casting and powder washing, a relative density of more than 63 vol% at green bodies was achieved. It was found that washing and repeated centrifugation of sterically stabilized powder improved dispersing of the powder in UV curable resin and significantly increased relative densities after sintering, resp. shifted sintering temperatures to lower temperatures which resulted in distinctive retardation of grains coarsening. This finally allowed reaching relative densities of 99.1 % with very fine and homogeneous microstructures with average grain sizes of 270 nm. It was further discovered that washing prior to sintering increased relative density after sintering as in case of powder washing with subsequent re-centrifuging.

Finally, HIP operations did not bring desirable effect in terms of significantly improved light transmittance through the sheets. This is due to the fact that a suitable HIP regime could not be used because of restricted possibilities. Therefore, eventually, only very low level of light transmission through the sheets was achieved. Finally, hardness measurements of sintered and HIPed specimens were performed resulting in HV2 > 21.5 GPa.

7. A list of used literature

[1]   A. Krell, J. Klimke, T. Hutzler. *Advanced spinel and sub-μm Al$_2$O$_3$ for transparent armour applications.* Journal of the European Ceramic Society, 2009, vol. 29, pp. 275-281.

[2]   P. J. Patel, G. Gilde and J. W. McCauley. *Transient liquid phase reactive sintering of aluminium oxynitride.* US Patent 7,045,091 B1, Int. Class. C04B35/10, 16.05.2006.

[3]   O. Yeheskel and O. Tevet. *Elastic moduli of transparent yttria.* Journal of the American Ceramic Society, 1999, vol. 82(1), pp. 136-144.

[4]   H. D. Lee, T. I. Mah, T. A. Parthasarathy and K. A. Keller. *YAG lasing systems and methods.* US Patent Application US 2005/0281302 A1, Int. Class. IPK[7] H01S3/16, 22.12.2005.

[5]   A. Krell, J. Klimke, T. Hutzler. *Transparent compact ceramics: Inherent physical issues.* Optical Materials, 2009, vol. 31, pp. 1144-1150.

[6]   A. Krell, P. Blank, H. Ma, T. Hutzler, M. P. B. van Bruggen, R. Apetz. *Transparent Sintered Corundum with High Hardness and Strength,* Journal of the American Ceramic Society. 2003, vol. 86(1), pp. 12-18.

[7]   A. Krell. *Improved hardness and hierarchic influences on wear in submicron sintered alumina.* Materials Science and Engineering: A, 1996, vol. 209(1-2), pp. 156-163.

[8]   A. Krell, T. Hutzler, J. Klimke. *Transmission physics and consequences for materials selection, manufacturing, and applications.* Journal of the European Ceramic Society, 2009, vol. 29, pp. 207-221.

[9]   R. Apetz, P. B. van Bruggen. *Transparent Alumina: A Light-Scattering Model.* Journal of the American Ceramic Society, 2003, vol. 86(3), pp. 480-486.

[10]   K. Hayashi, O. Kobayashi, S. Toyoda and K. Morinaga. *Transmission Optical Properties of Polycrystalline Alumina with Submicron Grains.* Mater. Trans. JIM, 1991, vol. 32, pp. 1024-1029.

[11]   J. G. J. Peelen. *Light Transmission of Sintered Alumina.* Phillips Tech. Rev., 1976, vol. 36, pp. 47-52.

[12] E. Glenn. *Refraction – The Physics Hypertextbook* [online]. Available at World Wide Web: < http://physics.info/refraction/>

[13] D. R. Askeland, P. P. Phulé. The Science and Engineering of Materials, 4th Edition, *Chapter 3 – Atomic and Ionic Arrangements* [online], pp. 75. Available at World Wide Web: <http://www.ccm.udel.edu/Personnel/homepage/class_web/ Lecture%20Notes/2004/askelandphulenotes-ch03printable.ppt>

[14] D. R. Ulrich. *Chemical processing of ceramics.* Chemical & Engineering News, January 1990, pp. 28-40.

[15] H. Rhodes. *Agglomerate and Particle Size Effects on Sintering Yttria-Stabilized Zirconia*. Journal of the American Ceramic Society, 1981, vol. 64(1), pp. 19-22.

[16] I. Aksay and C. H. Shilling. In *Ultrastructure Processing of Ceramic, Glasses and Composites* (L. L. Hench and D. R. Ulrich, eds.). John Wiley, New York, 1984, p. 439.

[17] F. F. Lange. *Powder processing science and technology for increased reliability*. Journal of the American Ceramic Society, 1989, vol. 72, pp. 3-15.

[18] I. A. Aksay. *Microstructure control through colloidal consolidation*, in *Advances in Ceramics*, vol. 9, Mangels J. A. and Messing G. L. (Eds), American Ceramics Society, Columbus, OH, 1984, pp. 94-104.

[19] R. J. Pugh, L. Bergström. *Surface and Colloid Chemistry in Advanced Ceramics Processing.* Surfactants science series, vol. 51. Marcel Dekker, New York, 1994, p. 363.

[20] L. Bergström. *Colloidal Processing of Ceramics*, in *Handbook of Applied Surface and Colloid Chemistry*. K. Holmberg (Edt). John Willey & Sons, Ltd, 2001.

[21] G. D. Parfitt. *Dispersion of Powders in Liquids*. John Wiley, New York, 1979.

[22] B. I. Lee, S. Komarneni. *Chemical Processing of Ceramics.* CRC Press, Taylor & Francis Group, 2005, p. 759.

[23] A. C. Pierre. *Introduction to Sol-Gel Processing*. Kluwer Academic Publishers, 1998, p. 297.

[24] J. L. Atwood, J. W. Steed. *Encyclopedia of Supramolecular Chemistry*. Marcel Dekker, New York, 2004, vol. 1, p. 899.

[25]   CustomPartNet 2008 [online]. Available at World Wide Web: http://www.custompartnet.com/wu/stereolithography

[26]   G. S. Upadhyaya. *Sintered Metallic and Ceramic Materials – Preparation, Properties and Applications.* John Willey & Sons Ltd, 1999, p. 670.

[27]   Y. DeHazan, T. Reuter, D. Werner, R. Clasen, T. Graule. *Interactions and dispersion stability of aluminum oxide colloidal particles in electroless nickel solutions in the presence of comb polyelectrolytes.* Journal of Colloid and Interface Science, 2008, vol. 323, pp. 293-300.

[28]   Y. DeHazan, J. Heinecke, A. Weber, T. Graule. *High solids loading ceramic colloidal dispersions in UV curable media via comb-polyelectrolyte surfactants.* Journal of Colloid and Interface Science, 2009, vol. 337, pp. 66-74.

[29]   M. Wozniak, T. Graule, Y. D. Hazan, D. Kata, J. Lis. *Highly loaded UV curable nanosilica dispersions for rapid prototyping applications.* Journal of the European Ceramic Society, 2009, vol. 29, pp. 2259–2265.

[30]   J. Heinecke. *Shaping of ceramic composite components from nano dispersions in UV curable resins.* Diploma thesis in ceramic processing. TU Clausthal, Germany, 2008, p. 85.

[31]   P. C. Hidber, T. J. Graule, L. J. Gauckler. *Citric Acid—A Dispersant for Aqueous Alumina Suspensions.* Journal of the American Ceramic Society, 1996, vol. 79, pp. 1857–1867.

[32]   C. Hinczewski, S. Corbel, T. Chartier, *Ceramic Suspensions Suitable for Stereolithography*, Journal of the European Ceramic Society, 1998, vol. 18, pp. 583-590.

[33]   A. Licciulli, C. Esposito Corcione, A. Greco, V. Amicarelli, A. Maffezzoli. *Laser stereolithography of ZrO_2 toughened Al_2O_3.* Journal of the European Ceramic Society, 2005, vol. 25, pp. 1581–1589.

[34]   T. M. Gabriel Chu, J. W. Halloran. *High-Temperature Flow Behavior of Ceramic Suspensions,* J. Am. Ceram. Soc., vol. 83, 2000, p. 2189-2195.

[35]   A. R. Studart, E. Amstad, M. Antoni, L. J. Gauckler. *Rheology of concentrated suspensions containing weakly attractive alumina nanoparticles.* Journal of the American Ceramic Society, 2006, vol. 89, pp. 2418-2425.

[36] K. Lu, Ch. S. Kessler, R. M. Davis. *Optimization of a Nanoparticle Suspension for Freeze Casting.* Journal of the American Ceramic Society, 2006, vol. 89, pp. 2459-2465.

[37] E. N. da C. Andrade. *The viscosity of liquids.* Nature, 1930, vol. 125, pp. 309-310.

[38] S. K. Glasstone, J. Laidler, H. Eyring. *The theory of rate process.* New York: McGraw-Hill, 1941.

[39] L. M. Griffith, J. W. Halloran. *Ultraviolet Curable Ceramic Suspensions for Stereo-lithography of Ceramics.* PED-vol. 68-2, Manufacturing Science and Engineering, 1994, vol. 2, pp. 529-534.

[40] L. M. Griffith, J. W. Halloran. *Freeform Fabrication of Ceramics via Stereolithography.* Journal of the American Ceramic Society, 1996, vol. 79, pp. 2601-2608.

[41] Y. DeHazan, M. Wozniak, J. Heinecke, G. Müller, T. Graule. *New Microshaping Concepts for Ceramic/Polymer Nanocomposite and Nanoceramic Fibers.* Journal of the American Ceramic Society, 2010, Vol. 93, pp. 2456–2459.

[42] T. Hanemann, K. Honnef, J. Hausselt. *Process chain development for the rapid prototyping of microstructured polymer, ceramic and metal parts: composite flow behaviour optimization, replication via reaction moulding and thermal postprocessing.* The International Journal of Advanced Manufacturing Technology, 2007, vol. 33, pp. 167-175.

[43] M. Mickoczyova, D. Galusek. *Influence of forming method and sintering process on densification and final microstructure of submicrometre alumina ceramics.* Processing and Application of Ceramics, 2008, vol. 2(1), pp. 13-17.

[44] D. S. Kim, J. H. Lee, R. J. Sung, S. W. Kim, H. S. Kim, J. S. Park. *Improvement of trans lucency in Al_2O_3 ceramics by two-step sintering technique.* Journal of the European Ceramic Society, 2007, vol. 27, pp. 3629-3632.

[45] K. Maca, V. Pouchly, Z. Shen. *Two-Step Sintering and Spark Plasma Sintering of Al_2O_3, ZrO_2 and $SrTiO_3$ Ceramics.* Integrated Ferroelectrics, 2008, vol. 99, pp. 114-124.

1. General table

solid load. with dispersant	monomers type BDMA+M292	ratio	amount	photoinitiator type	amount (5 wt.%)	UV curing time per layer	sample thickness [mm]	debinding heating rate °C / min	temp. [°C]	rel. density of GB	sintering heating rate °C/min	temp./dwell time °C / h	rel. density of SB	microstructure average grain size	homogenity	final porosity open	close
57 vol.%	√	14:1	43 vol.%	LTM	√	2'	1	0.5	650	61.5 %	5	1350/6h	94.6 %	250 nm	Very good	0.2%	5.2%
57 vol.% non-degassed	√	14:1	43 vol.%	LTM	√	2'	1	0.5	650	60.3 %	5	1350/6h	92.9 %	250 nm	Very good	0.4%	6.7%
57 vol.% multi-layer	√	14:1	43 vol.%	LTM	√	1'	4x0.25	0.5 / split layers	650	61.0 %	5	1350/6h	97.4 %	250 nm	Very good	0.2%	2.4%
57 vol.%	√	14:1	43 vol.%	LTM	√	2'	1	10	800	-	5	1300/2h	84 %	-	Very good	16%	0%
57 vol.%	√	14:1	43 vol.%	LTM	√	2'	1	0.9	650/2h	61.9 %	1.4	1500/2h	96.3 %	510 nm	poor	0.7%	3%
57 vol.%	√	14:1	43 vol.%	LTM	√	2'	1	0.5	650	61.5 %	5	1450/11h	96.9 %	1550 nm	Very poor	0.0%	3.1%
57 vol.% non-degassed	√	14:1	43 vol.%	LTM	√	2'	1	0.5	650	60.3 %	5	1450/11h	93.7 %	1440 nm	Very poor	0.0%	6.3%
57 vol.% multi-layer	√	14:1	43 vol.%	LTM	√	1'	4x0.25	0.5 / split layers	650	61.0 %	5	1450/11h	98.8 %	1400 nm	Very poor	0.0%	1.2%
57 vol.% multi-layer	√	14:1	43 vol.%	LTM	√	1'	4x0.25	0.5	650	61.0 %	5	1450/6h	96.6 %	690 nm	poor	0.0%	3.4%
57 vol.%	√	14:1	43 vol.%	LTM	√	2'	1	0.5	650	61.5 %	5	1450/6h	97.9 %	800 nm	Very poor	0.0%	2.1%
57 vol.%	√	14:1	43 vol.%	LTM	√	2'	1	5	-	-	5	1450/6h	93.8 %	810 nm	Very poor	0.0%	6.2%

57 vol.% multi-layer	√	14:1	43 vol.%	LTM	√	1'	4x0.25	5	-	-	5	1450/6h	**96.5 %**	**720 nm**	poor	**0.0%**	3.5%
57 vol.% non-degassed	√	14:1	43 vol.%	LTM	√	2'	1	0.5	650	60.3 %	5	1450/6h	**94.6 %**	**840 nm**	Very poor	**0.0%**	5.4%
57 vol.% non-degassed	√	14:1	43 vol.%	LTM	√	2'	1	5	-	-	5	1450/6h	**92.0 %**	**890 nm**	Very poor	**0.0%**	8.0%
57 vol.% non-degassed	√	14:1	43 vol.%	MBF	√	2'	1	HR: 1°C/min 400°C / 2h		-	5	1350/6	**93.8 %**	**320 nm**	Very good	**0.7%**	5.5%
57 vol.% multi-layer non- degassed	√	14:1	43 vol.%	MBF	√	1'	4x0.25	HR: 1°C/min 400°C / 2h		-	5	1350/6	**96.5 %**	**345 nm**	good	**0.0%**	3.5%
57 vol.% non-degassed	√	14:1	43 vol.%	1.25 TPO	√	2'	1	HR: 1°C/min 400°C / 2h		-	5	1350/6	**90.7%**	**245 nm**	Very good	**1.9%**	7.4%
57 vol.% multi-layer non- degassed	√	14:1	43 vol.%	1.25 TPO	√	1'	4x0.25	HR: 1°C/min 400°C / 2h		-	5	1350/6	**92.1%**	**320 nm**	Very good	**1.3%**	6.7%
57 vol.% non-degassed	√	14:1	43 vol.%	LTM	√	2'	1	HR: 1°C/min 400°C / 2h		-	5	1350/6	**90.4 %**	**310 nm**	Very good	**1.9%**	7.7%
57 vol.% multi-layer non- degassed	√	14:1	43 vol.%	LTM	√	1'	4x0.25	HR: 1°C/min 400°C / 2h		-	5	1350/6	**91.7%**	**320 nm**	good	**1.0%**	7.3%
57 vol.% multi-layer non- degassed	√	14:1	43 vol.%	MBF	√	1'	4x0.25	HR: 0.5°C/min 400°C / 7h,400-550 (2°C/min)		58.7 %							
57 vol.% multi-layer sieved 27.5.2010	√	14:1	43 vol.%	MBF	√	2'	4x0.25	HR: 0.5°C/min 400°C / 7h,400-550 (2°C/min)		61.5 %	RT-800 10°C/min 800-1400 5°C/min 1400-1200 20°C/min 1200-dwell time 20 h 1200-RT 5°C/min		**90 %**			**5.0%**	5.0%

57 vol.% 27.5.2010	√	14:1	43 vol.%	LTM	√	2'	1	0.5	650	61.5 %	RT-800 10°C/min 800-1400 5°C/min 1400-1200 20°C/min 1200-dwell time 20 h 1200-RT 5°C/min	**90.6 %**			**8.1%**	1.3%
57 vol.% multi-layer sieved 27.5.2010	√	14:1	43 vol.%	MBF	√	2'	4x0.25	HR: 0.5°C/min 400°C / 7h,400-550 (2°C/min)		61.5 %	RT-800 10°C/min 800-dwell time 40 h 800-1350 5°C/min 1350 dwell time 6 h 1350-RT 5°C/min	**96 %**	**320 nm**	Very good	**0.0%**	4.0%
57 vol.% 27.5.2010	√	14:1	43 vol.%	LTM	√	2'	1	0.5	650	61.5 %	RT-800 10°C/min 800-dwell time 40 h 800-1350 5°C/min 1350 dwell time 6 h 1350-RT 5°C/min	**94.1%**			**0.0%**	5.9%
TS: 57 vol.% multi-layer sieved 1.6.2010	√	14:1	43 vol.%	MBF	√	2'	4x0.25	HR: 0.5°C/min 400°C / 7h,400-550 (2°C/min)		61.5 %	RT - 800/10, 800 - 1500/5, 1500 - 1350/20, 1350 - 6h, 1350 - RT/5	**98.85 %**	**455 nm**	good	**0.0%**	1.15%
TS: 57 vol.% multi-layer sieved 1.6.2010	√	14:1	43 vol.%	MBF	√	2'	4x0.25	HR: 0.5°C/min 400°C / 7h,400-550 (2°C/min)		61.5 %	RT-800 10°C/min 800-1400 5°C/min 1400-1200 20°C/min 1200-dwell time 20 h 1200-RT 5°C/min RT - 800/10, 800 - 1500/5, 1500 - 1350/20, 1350 - 6h, 1350 - RT/5.	**98.05%**	**425 nm**	Very good	**0.0%**	2%
PC+TS: 57 vol.% multi-layer sieved 1.6.2010	√	14:1	43 vol.%	MBF	√	2'	4x0.25	HR: 0.5°C/min 400°C / 7h,400-550 (2°C/min)		61.5 %	RT-800 (10°C/min), 800 - 40h, 800 -1350 (5°C/min), 1350 - 6h, 1350 - RT (5°C/min) + RT - 800/10, 800 - 1500/5, 1500 - 1350/20, 1350 - 6h,	**97.57%**	**335 nm**	Very good	**0.0%**	2.4%

											1350 - RT/5.					
57 vol.% multi-layer sieved 1.6.2010	√	14:1	43 vol.%	MBF	√	2'	4x0.25	HR: 0.5°C/min 400°C / 7h,400-550 (2°C/min)		61.5 %	RT/1400/10, 1400-6h, 1400/RT/10	**99.46%**	**425 nm**	Very good	**0,0%**	0.54%
57 vol.% multi-layer sieved 14.6.2010	√	14:1	43 vol.%	LTM	√	2'	4x0.25	0.5	650	61.6 %	RT/1400/10, 1400-6h, 1400/RT/10	**96.18%**	**440 nm**	Very good	**0.0%**	3.8%
57 vol.% multi-layer sieved 16.6.2010	√	14:1	43 vol.%	MBF	√	2'	4x0.25	HR: 0.5°C/min 400°C / 7h,400-550 (2°C/min)		61.5 %	RT/1500/10, 1500/1400/50, 1400-6h, 1400/RT/10	**98.8%**	**480 nm**	good	**0,0%**	1.2%
57 vol.% multi-layer sieved 16.6.2010	√	14:1	43 vol.%	LTM	√	2'	4x0.25	0.5	650	61.6 %	RT/1500/10, 1500/1400/50, 1400-6h, 1400/RT/10	**95.6%**	**415 nm**	good	**0.0%**	4.4%
PC: 57 vol.% multi-layer sieved 18.6.2010	√	14:1	43 vol.%	MBF	√	2'	4x0.25	HR: 0.5°C/min 400°C / 7h,400-550 (2°C/min)		61.5 %	RT/1000/20, 1000 - 20h, 1000/1400/10, 1400-6h, 1400/RT/10	**99.0%**	**510 nm**	good	**0.0%**	1%
57 vol.% multi-layer sieved 18.6.2010	√	14:1	43 vol.%	LTM	√	2'	4x0.25	0.5	650	61.6 %	RT/1000/20, 1000 - 20h, 1000/1400/10, 1400-6h, 1400/RT/10	**95.0%**	**475 nm**	good	**0.0%**	5%
57 vol.% multi-layer sieved 21.6.2010	√	14:1	43 vol.%	MBF	√	2'	4x0.25	0.5	650	62.4 %	RT/1400/10, 1400-6h, 1400/RT/10	**98.84%**	**415 nm**	good	**0.0%**	1.2%
57 vol.% multi-layer	√	14:1	43 vol.%	LTM	√	2'	4x0.25	0.5	650	61.6 %	RT/1400/10, 1400-6h, 1400/RT/10	**94.15%**	**430 nm**	poor	**0.0%**	5.8%

71

sieved 21.6.2010																
57 vol.% multi-layer sieved 22.6.2010 Archimedes	√	14:1	43 vol.%	MBF	√	2'	4x0.25	0.5	650	62.4 %	RT/1350/10, 1350-6h, 1350/RT/10	**98.76%**	**225 nm**	Very good	**0.0%**	1.2%
57 vol.% multi-layer sieved 22.6.2010	√	14:1	43 vol.%	MBF	√	2'	4x0.25	0.5	650	62.4 %	RT/1350/10, 1350-6h, 1350/RT/10	**97.78%**	**275 nm**	Very good	**0.0%**	2.2%
57 vol.% multi-layer sieved 23.6.2010 Archimedes	√	14:1	43 vol.%	MBF	√	2'	4x0.25	0.5	650	63.1 %	RT/1350/10, 1350-6h, 1350/RT/10	**98.43%**	**-**	Very good	**0.0%**	1.6%
57 vol.% multi-layer sieved 23.6.2010	√	14:1	43 vol.%	MBF	√	2'	4x0.25	0.5	650	63.1 %	RT/1350/10, 1350-6h, 1350/RT/10	**96.89%**	**-**	Very good	**0.0%**	3.1%
57 vol.% multi-layer sieved 29.6.2010 Archimedes-N.B.	√	14:1	43 vol.%	MBF	√	2'	4x0.25	0.5	650	63.7 %	RT/1375/10, 1375-6h, 1375/RT/10	**99.00%**	**245 nm**	Very good	**0.0%**	1%
57 vol.% multi-layer sieved 29.6.2010 N.B.	√	14:1	43 vol.%	MBF	√	2'	4x0.25	0.5	650	63.7 %	RT/1375/10, 1375-6h, 1375/RT/10	**98.3%**	**340 nm**	good	**0.0%**	1.7%
57 vol.% multi-layer sieved 29.6.2010 Archimedes O.B.	√	14:1	43 vol.%	MBF	√	2'	4x0.25	0.5	650	63.0 %	RT/1375/10, 1375-6h, 1375/RT/10	**98.6%**	**380 nm**	good	**0.0%**	1.4%

57 vol.% multi-layer sieved 29.6.2010 O.B.	√	14:1	43 vol.%	MBF	√	2'	4x0.25	0.5	650	63.0 %	RT/1375/10, 1375-6h, 1375/RT/10	**98.3%**	**250 nm**	good	**0.0%**	1.7%
57 vol.% 4 layers sieved 6.7.2010 Archimedes N.B.	√	14:1	43 vol.%	MBF	√	2'	4x0.25	0.5	650	63.7 %	RT/1350/10, 1350-9h, 1350/RT/10	**97.8%**	**250 nm**	Very good	**0.0%**	2.2%
57 vol.% 2 layers sieved 6.7.2010 Archimedes N.B.	√	14:1	43 vol.%	MBF	√	2'	2x0.25	0.5	650	63.7 %	RT/1350/10, 1350-9h, 1350/RT/10	**97.4%**	**230 nm**	Ver ygood	**0.0%**	2.6%
57 vol.% 4 layers sieved 6.7.2010 N.B.	√	14:1	43 vol.%	MBF	√	2'	4x0.25	0.5	650	63.7 %	RT/1350/10, 1350-9h, 1350/RT/10	**95.4%**	**245 nm**	good	**0.0%**	4.6%
57 vol.% 4 layers sieved 19.7.2010 washed powder Archimedes	√	14:1	43 vol.%	MBF	√	2'	4x0.25	0.5	650	62.6 %	RT/1350/10, 1350-6h, 1350/RT/10	**99.1%**	**270 nm**	Very good	**0.0%**	0.9%
57 vol.% 4 layers sieved 19.7.2010 washed powder	√	14:1	43 vol.%	MBF	√	2'	4x0.25	0.5	650	62.6 %	RT/1350/10, 1350-6h, 1350/RT/10	**98.4%**	**250 nm**	Very good	**0.0%**	1.6%
57 vol.% 4 layers sieved 19.7.2010 Archimedes N.B.	√	14:1	43 vol.%	MBF	√	2'	4x0.25	0.5	650	63.7 %	RT/1350/10, 1350-6h, 1350/RT/10	**99.0%**	**265 nm**	Very good	**0.0%**	1.0%

|																	
57 vol.% 4 layers sieved 19.7.2010 N.B.	√	14:1	43 vol.%	MBF	√	2'	4x0.25	0.5	650	63.7 %	RT/1350/10, 1350-6h, 1350/RT/10		**95.8%**	**290 nm**	Very good	**0.0%**	1.0%
57 vol.% 4 layers sieved 19.7.2010 O.B.	√	14:1	43 vol.%	MBF	√	2'	4x0.25	0.5	650	63.0 %	RT/1350/10, 1350-6h, 1350/RT/10		**97.0%**	**270 nm**	Very good	**0.0%**	3.0%
57 vol.% 4 layers sieved 19.7.2010 Archimedes O.B.	√	14:1	43 vol.%	MBF	√	2'	4x0.25	0.5	650	63.0 %	RT/1350/10, 1350-6h, 1350/RT/10		**98.4%**	**260 nm**	Very good	**0.0%**	1.6%
50 vol.% non-degassed	√	14:1	50 vol.%	LTM	√	2'	1	0.5	650	56 %	5	1450/11h	**95.4%**	**1470 nm**	Very poor	**0.0%**	4.6%
42 vol.%	√	14:1	58 vol.%	LTM	√	2'	1	0.5	650	50.8 %	5	1350/2h	**82.6%**	**-**	-	**16.6%**	0.8%
42 vol.% non-degassed	√	14:1	58 vol.%	LTM	√	2'	1	0.5	650	55 %	5	1350/2h	**88.4 %**	**-**	-	**9.5%**	2.1%
42 vol.%	√	14:1	58 vol.%	LTM	√	2'	1	0.5	650	50.8%	5	1450/11h	**95.3 %**	**2000 nm**	Very poor	**0.0%**	4.7%
42 vol.% non-degassed	√	14:1	58 vol.%	LTM	√	2'	1	0.5	650	55 %	5	1450/11h	**93.6 %**	**1200 nm**	poor	**0.0%**	6.4%

2. SEM pictures

Fracture section of a multilayer sintered sheet made out of sieved ceramic suspension.
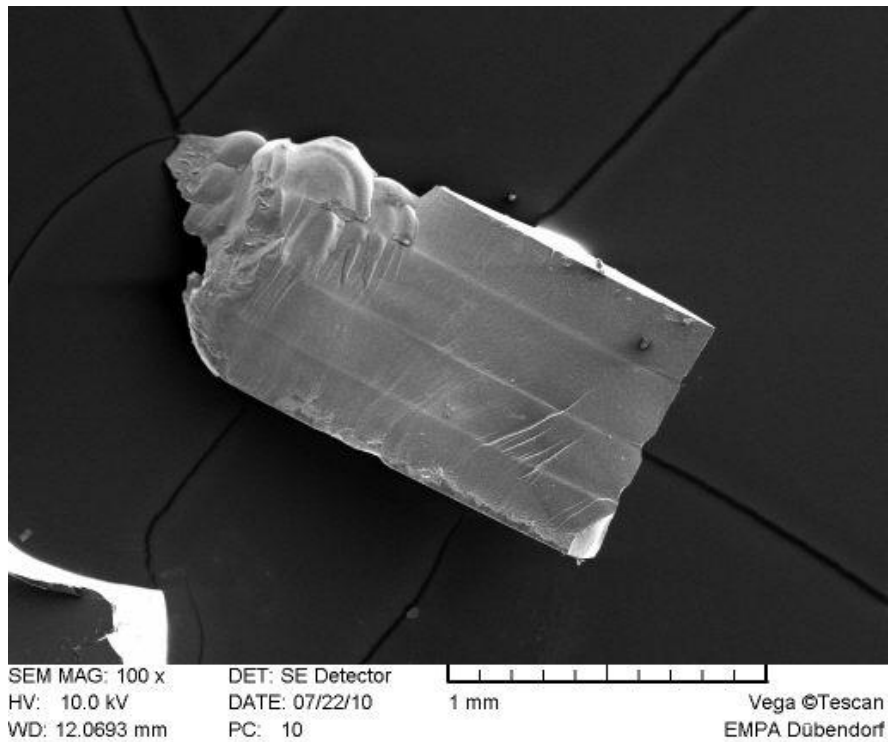
Fracture section of a monolayer sintered sheet made out of non degassed ceramic suspension.
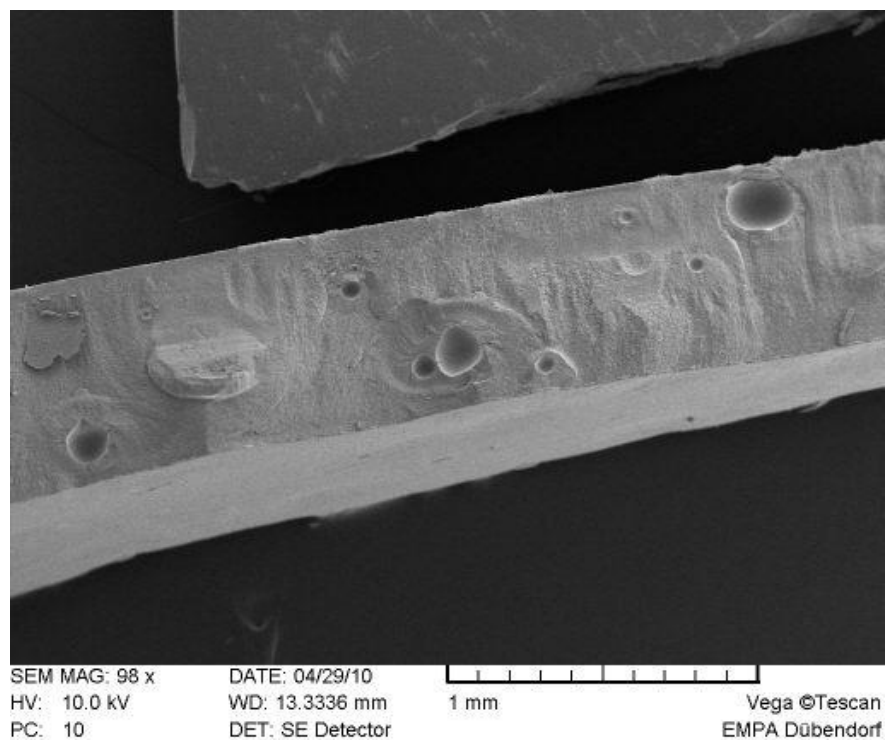
Fracture section of a sample submitted to two-step sintering with following sintering regime: RT-800/10, 800-1500/5, 1500-1350/20, 1350-6 h, 1350-RT/5. Relative density 98.85 %.
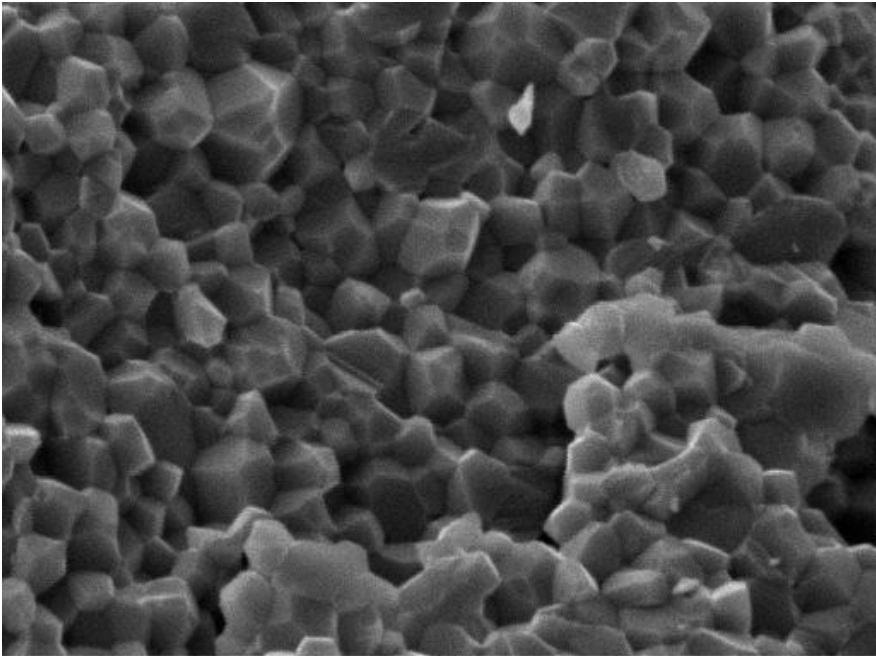
SEM MAG: 22.37 kx   DET: SE Detector
HV: 10.0 kV   DATE: 06/14/10   5 um   Vega ©Tescan
WD: 12.1228 mm   PC: 16   EMPA Dübendorf